

Supporting Information

Precision N-Species Engineering in Pt–N₄ via Ring-Reconstruction towards Efficient Alkaline Water Electrolysis

By Liu *et al.*

Contents

Materials	5
Apparatus and measurements	5
Electrochemical measurements	5
Activation energy (E_a) calculation	6
AEMWE Test	7
In situ surface-enhanced Raman spectroscopy measurements.	7
Theoretical calculations	8
Synthesis of ZIF-8@ZIF-67	9
Synthesis of Co_n@N_[6]C	9
Synthesis of Co_n@N_{[5]/[6]}C	9
Synthesis of Co_n-Pt₁@N_{[5]/[6]}C and Co_n-Pt₁@N_[6]C	9
Fig. S1. Three possible initial structures of N _{[5]/[6]} C configurations are depicted alongside their corresponding DFT optimized structural models, with the relative electronic energies of the DFT optimized structures provided.....	11
Fig. S2. Optimized H* adsorption structures of Pt ₁ @N _[6] C, Pt ₁ @N _{[5]/[6]} C, and Pt ₁ @N _[5] C.	11
Fig. S3. Calculated PDOS of Pt 5d for Pt ₁ @N _[6] C, Pt ₁ @N _{[5]/[6]} C, and Pt ₁ @N _[5] C.	12
Fig. S4. High-resolution XPS N 1s spectra of ZIF-67 pyrolysis products in H ₂ /Ar and Ar.....	12
Fig. S5. The function of Co _n : (a) Catalyzing hydrogenation reaction; (b) Severing as OH* adsorption site .	13
Fig. S6. (a) Schematic models and (b) reaction energy barrier of Co _n -incorporated <i>vs.</i> Co-free systems....	13
Fig. S7. SEM image of core-shell ZIF-8@ZIF-67.	14
Fig. S8. TEM images of core-shell ZIF-8@ZIF-67.	14
Fig. S9. STEM image and energy-dispersive X-ray spectroscopy (EDS) element mapping of core-shell ZIF-8@ZIF-67.	14
Fig. S10. Binding energies between Co _n -N _{[5]/[6]} C, Co _n -N _[6] C, and Co _n -N _[5] C and Pt (Inset: Structure models of Co _n -Pt ₁ @N _{[5]/[6]} C, Co _n -Pt ₁ @N _[6] C, and Co _n -Pt ₁ @N _[5] C). Note that Co _n -N _[5] C exhibits positive binding energy towards Pt ₁ , suggesting the poor stability of Co _n -Pt ₁ @N _[5] C.	15
Fig. S11. Bader charge of Pt and N in Co _n -Pt ₁ @N _{[5]/[6]} C, Co _n -Pt ₁ @N _[6] C, and Co _n -Pt ₁ @N _[5] C.	15

Fig. S12. Screening process for $\text{Co}_n\text{-Pt}_1@\text{N}_{[5]} \text{C}$ models by DFT.....	16
Fig. S13. Gibbs free energy of H^* adsorption on $\text{Co}_n\text{-Pt}_1@\text{N}_{[5]/[6]} \text{C}$, $\text{Co}_n\text{-Pt}_1@\text{N}_{[6]} \text{C}$, and $\text{Co}_n\text{-Pt}_1@\text{N}_{[5]} \text{C}$..	16
Fig. S14. Corresponding contents of $\text{N}_{[6]}$, $\text{N}_{[5]}$, M-N, G-N, and O-N in $\text{Co}_n\text{-Pt}_1@\text{N}_{[5]/[6]} \text{C}$ and $\text{Co}_n\text{-Pt}_1@\text{N}_{[6]} \text{C}$. ..	17
Fig. S15. XRD pattern of (a) $\text{Co}_n\text{-N}_{[5]/[6]} \text{C}$, $\text{Co}_n\text{-N}_{[6]} \text{C}$, $\text{Co}_n\text{-Pt}_1@\text{N}_{[5]/[6]} \text{C}$, and $\text{Co}_n\text{-Pt}_1@\text{N}_{[6]} \text{C}$; and (b) $\text{Co}_c\text{-N}_{[5]/[6]} \text{C}$, $\text{Co}_c\text{-N}_{[6]} \text{C}$, $\text{Co}_c\text{-Pt}_1@\text{N}_{[5]/[6]} \text{C}$, and $\text{Co}_c\text{-Pt}_1@\text{N}_{[6]} \text{C}$. ..	17
Fig. S16. TEM images of $\text{Co}_c\text{-Pt}_1@\text{N}_{[5]/[6]} \text{C}$	17
Fig. S17. TEM images of $\text{Co}_c\text{-Pt}_1@\text{N}_{[6]} \text{C}$. ..	18
Fig. S18. High-resolution XPS spectra of Co 2p for (a) $\text{Co}_n\text{-N}_{[5]/[6]} \text{C}$ and $\text{Co}_n\text{-N}_{[6]} \text{C}$, (b) High-resolution XPS spectra of Co 2p $\text{Co}_n\text{-Pt}_1@\text{N}_{[5]/[6]} \text{C}$ and $\text{Co}_n\text{-Pt}_1@\text{N}_{[6]} \text{C}$, (c) $\text{Co}_c\text{-N}_{[5]/[6]} \text{C}$ and $\text{Co}_c\text{-N}_{[6]} \text{C}$, (d) $\text{Co}_c\text{-Pt}_1@\text{N}_{[5]/[6]} \text{C}$ and $\text{Co}_c\text{-Pt}_1@\text{N}_{[6]} \text{C}$. ..	18
Fig. S19. XPS spectra of N 1s for $\text{Co}_c\text{-N}_{[5]/[6]} \text{C}$ and $\text{Co}_c\text{-N}_{[6]} \text{C}$	19
Fig. S20. XPS spectra of N 1s for $\text{Co}_c\text{-Pt}_1@\text{N}_{[5]/[6]} \text{C}$ and $\text{Co}_c\text{-Pt}_1@\text{N}_{[6]} \text{C}$. ..	19
Fig. S21. High-resolution XPS spectra of Pt 4f.....	20
Fig. S22. Fourier-transformed magnitude of Pt L ₃ EXAFS spectra in K space, (a) $\text{Co}_n\text{-Pt}_1@\text{N}_{[5]/[6]} \text{C}$, (b) $\text{Co}_n\text{-Pt}_1@\text{N}_{[6]} \text{C}$, (c) Pt foil, (d) PtO_2	21
Fig. S23. Fourier-transformed magnitude of Pt L ₃ EXAFS spectra in R space. (a) $\text{Co}_n\text{-Pt}_1@\text{N}_{[5]/[6]} \text{C}$, (b) $\text{Co}_n\text{-Pt}_1@\text{N}_{[6]} \text{C}$, (c) Pt foil.....	21
Fig. S24. (a) wavelet-transformed k ² -weighted EXAFS spectra of $\text{Co}_n\text{-Pt}_1@\text{N}_{[5]/[6]} \text{C}$, (b) $\text{Co}_n\text{-Pt}_1@\text{N}_{[6]} \text{C}$, (c) Pt foil, and (d) PtO_2 . ..	22
Fig. S25. SEM images of $\text{Co}_n\text{-N}_{[5]/[6]} \text{C}$	22
Fig. S26. SEM images of $\text{Co}_n\text{-N}_{[6]} \text{C}$	22
Fig. S27. SEM images of $\text{Co}_n\text{-Pt}_1@\text{N}_{[5]/[6]} \text{C}$	23
Fig. S28. SEM images of $\text{Co}_n\text{-Pt}_1@\text{N}_{[6]} \text{C}$. ..	23
Fig. S29. TEM images of $\text{Co}_n\text{-N}_{[5]/[6]} \text{C}$	23
Fig. S30. TEM images of $\text{Co}_n\text{-N}_{[6]} \text{C}$. The internal structure did not undergo significant collapse, indicating that the Co_n may be encapsulated by the carbon layers.....	23
Fig. S31. TEM images of $\text{Co}_n\text{-Pt}_1@\text{N}_{[5]/[6]} \text{C}$	24
Fig. S32. STEM images and EDS mapping of $\text{Co}_n\text{-Pt}_1@\text{N}_{[5]/[6]} \text{C}$. ..	24
Fig. S33. TEM (a, b) and HRTEM (c) images of $\text{Co}_n\text{-Pt}_1@\text{N}_{[6]} \text{C}$. ..	24
Fig. S34. STEM images and EDS mapping of $\text{Co}_n\text{-Pt}_1@\text{N}_{[6]} \text{C}$	25
Fig. S35. (a) N_2 adsorption-desorption isotherm curves and (b) corresponding pore distributions of $\text{Co}_n\text{-N}_{[5]/[6]} \text{C}$ and $\text{Co}_n\text{-N}_{[6]} \text{C}$. ..	25

Fig. S36. (a) N_2 adsorption-desorption isotherm curves and (b) corresponding pore distributions of $Co_n\text{-}Pt_1\text{-}N_{[5]/[6]}C$ and $Co_n\text{-}Pt_1\text{-}N_{[6]}C$	25
Fig. S37. HAADF-STEM images of $Co_n\text{-}Pt_1\text{@}N_{[5]/[6]}C$	26
Fig. S38. HAADF-STEM images of $Co_n\text{-}Pt_1\text{@}N_{[5]/[6]}C$	26
Fig. S39. HAADF-STEM images of $Co_n\text{-}Pt_1\text{@}N_{[5]/[6]}C$	27
Fig. S40. HAADF-STEM images of $Co_n\text{-}Pt_1\text{@}N_{[5]/[6]}C$	27
Fig. S41. HAADF-STEM images of $Co_n\text{-}Pt_1\text{@}N_{[6]}C$	28
Fig. S42. HAADF-STEM images of $Co_n\text{-}Pt_1\text{@}N_{[6]}C$	28
Fig. S43. HAADF-STEM images of $Co_n\text{-}Pt_1\text{@}N_{[6]}C$	29
Fig. S44. HAADF-STEM images of $Co_n\text{-}Pt_1\text{@}N_{[6]}C$	29
Fig. S45. Potential calibration of the reference electrode concerning reversible hydrogen electrode (RHE).	30
Fig. S46. HER polarization curves of $Co_n\text{-}Pt_1\text{@}N_{[5]/[6]}C$ and $Co_n\text{-}N_{[5]/[6]}C$	30
Fig. S47. CV curves of (a) $Co_n\text{-}Pt_1\text{@}N_{[5]/[6]}C$ (b) $Co_n\text{-}Pt_1\text{@}N_{[6]}C$, (c) 20% Pt/C at different scanning rates, (d) The calculated C_{dl} for three catalysts.....	31
Fig. S48. Electrochemical impedance spectroscopy (EIS) curve of $Co_n\text{-}Pt_1\text{@}N_{[5]/[6]}C$, 20%Pt/C, and $Co_n\text{-}Pt_1\text{@}N_{[6]}C$	31
Fig. S49. The equivalent circuits for HER of $Co_n\text{-}Pt_1\text{@}N_{[5]/[6]}C$ in 1 M KOH (Tafel slope < 30). ¹⁵	31
Fig. S50. The equivalent circuits for HER of catalysis in 1 M KOH (Tafel slope>30).	32
Fig. S51 (a) Cyclic voltammetry curves of $Co_n\text{-}Pt_1\text{@}N_{[5]/[6]}C$, $Co_n\text{-}Pt_1\text{@}N_{[6]}C$, and Pt/C in Ar-saturated 1 M KOH with a scan rate of 50 mV s ⁻¹ ; (b) j_{ECFA} of various catalysts as a function of applied potential.....	33
Fig. S52. TEM (a, b), EDS mapping (c), and (d) HRTEM images of $Co_n\text{-}Pt_1\text{@}N_{[5]/[6]}C$ after 100 h stability testing.	33
Fig. S53. XRD patterns of 100 h-stability-tested $Co_n\text{-}Pt_1\text{@}N_{[5]/[6]}C$ and pristine carbon paper.....	34
Fig. S54. HER performance of $Co_c\text{-}Pt_1\text{@}N_{[5]/[6]}C$, 20%Pt/C, and $Co_c\text{-}Pt_1\text{@}N_{[6]}C$ in alkaline. (a) HER polarization curves, (b) Tafel plots, (c) CV curves of $Co_c\text{-}Pt_1\text{@}N_{[5]/[6]}C$, (d) CV curves of $Co_c\text{-}Pt_1\text{@}N_{[6]}C$ at different scan rates, (e) Corresponding evaluation of C_{dl} values, (f) EIS curves.....	34
Fig. S55. Polarization curves (a, c) and Tafel plots (b, d) under a certain temperature range of 25-50 °C for $Co_n\text{-}Pt_1\text{@}N_{[5]/[6]}C$ and $Co_n\text{-}Pt_1\text{@}N_{[6]}C$, respectively.	35
Fig. S56. <i>In-situ</i> electrochemical Raman spectra of interface adsorbed water at $Co_n\text{-}Pt_1\text{@}N_{[5]/[6]}C$ surface..	35
Fig. S57. <i>In-situ</i> Raman spectra electrochemical Raman spectra of interface adsorbed water at $Co_n\text{-}Pt_1\text{@}N_{[6]}C$ surface.	36
Fig. S58. Raman area ratios of the (a) 4HB-H ₂ O and (b) free-H ₂ O at $Co_n\text{-}Pt_1\text{@}N_{[5]/[6]}C$ and $Co_n\text{-}Pt_1\text{@}N_{[6]}C$ surface.	36

Fig. S59. TEM images (a-c) and EDS elemental mappings (d-f) of $\text{Co}_n\text{-Pt}_1@\text{N}_{[5]/[6]}\text{C}$ after 400 h AEMWE stability testing.....	37
Fig. S60. (a) High-resolution XPS spectra of N 1s for $\text{Co}_n\text{-Pt}_1@\text{N}_{[5]/[6]}\text{C}$ after 400 h AEMWE stability testing. (b) Corresponding contents of $\text{N}_{[6]}$, $\text{N}_{[5]}$, G-N, and O-N in $\text{Co}_n\text{-Pt}_1@\text{N}_{[5]/[6]}\text{C}$	37
Fig. S61. High-resolution XPS spectra of Pt 4f for $\text{Co}_n\text{-Pt}_1@\text{N}_{[5]/[6]}\text{C}$ after 400 h AEMWE stability testing.....	38
Fig. S62. High-resolution XPS spectra of Co 2p for $\text{Co}_n\text{-Pt}_1@\text{N}_{[5]/[6]}\text{C}$ after 400 h AEMWE stability testing.....	38
Fig. S63. Gibbs free energy diagram of the alkaline HER process on $\text{Co}_n\text{-Pt}_1@\text{N}_{[5]}\text{C}$	39
Fig. S64. Calculated PDOS of Pt 5d for $\text{Co}_n\text{-Pt}_1@\text{N}_{[5]/[6]}\text{C}$, $\text{Co}_n\text{-Pt}_1@\text{N}_{[6]}\text{C}$, and $\text{Co}_n\text{-Pt}_1@\text{N}_{[5]}\text{C}$. The d-band center of Pt in $\text{Co}_n\text{-Pt}_1@\text{N}_{[5]}\text{C}$ is significantly close to the Fermi level, indicating extremely strong H^* adsorption, which could impede the desorption of H^*	39
Fig. S65. Differential charge density image of water adsorption on $\text{Co}_n\text{-Pt}_1@\text{N}_{[5]}\text{C}$; the yellow and blue regions represent charge accumulation and decrease, respectively.....	40
Fig. S66. Water splitting model for $\text{Co}_n\text{-Pt}_1@\text{N}_{[5]}\text{C}$. The white, gray, blue, red, purple, and orange spheres represent H, C, N, O, Co, and Pt atoms, respectively. Due to the instability of this structure, it underwent degradation during the water-splitting process.....	40
Table S1. Recent advances in the regulation of types of N in single-atom catalysts.....	41
Table S2. Structural parameters of Pt foil and $\text{Co}_n\text{-Pt}_1@\text{NC}$ extracted from the EXAFS fitting	42
Table S3. Specific surface area, pore volume, and pore diameter information of $\text{Co}_n@\text{N}_{5/6}\text{C}$, $\text{Co}_n@\text{N}_6\text{C}$, $\text{Co}_n\text{-Pt}_1@\text{N}_{5/6}\text{C}$, and $\text{Co}_n\text{-Pt}_1@\text{N}_6\text{C}$	42
Table S4. Optimum fit parameters for the impedance data during HER in 1 M KOH.....	43
Table S5. Comparison of the HER performance with other state-of-the-art noble-metal single-atom HER electrocatalysts in alkaline.....	44
Table S6. Quantitative ICP-OES analysis of Co loading in $\text{Co}_n @\text{NC}$ and $\text{Co}_n\text{-Pt}_1@\text{NC}$	45
Table S7. Comparison of AEMWE cell voltages using different cathodic catalysts.....	45

Materials

All chemicals were used as received. Analytical grade zinc nitrate hexahydrate ($\text{Zn}(\text{NO}_3)_2 \cdot 6\text{H}_2\text{O}$), Cobalt(II) nitrate hexahydrate ($\text{Co}(\text{NO}_3)_2 \cdot 6\text{H}_2\text{O}$), 2-Methylimidazole, Chloroplatinic acid hexahydrate ($\text{H}_2\text{PtCl}_6 \cdot 6\text{H}_2\text{O}$) and Nafion (20%) were purchased from Aladdin Reagents Co., Ltd. Methanol (CH_3OH), Ethanol ($\text{C}_2\text{H}_5\text{OH}$), potassium hydroxide (KOH), and sulphuric acid (H_2SO_4) were purchased from Sinopharm Chemical Reagent Co., Ltd. The commercial Pt/C (20 wt.%) was purchased from Johnson Matthey. Ultrapure water with a resistance of $18.25 \text{ M}\Omega \text{ cm}^{-1}$ was made by a water purification machine in our lab. All the reagents and solvents were used as received, without further purification.

Apparatus and measurements

The morphology of samples was characterized by FE-SEM (JSM-6700F, accelerating voltage of 5 kV), HRTEM (JEM-2010, accelerating voltage of 200 kV), and high-angle annular dark-field scanning transmission electron microscopy (JEOL JEM-ARM200F TEM, accelerating voltage of 200 kV). EDS data were collected on an X-MaxN100TLE detector. The crystalline structures of as-synthesized materials were measured by X-ray diffraction (XRD; DX-2700 Xray diffractometer), Cu K α radiation, ($\lambda=1.5406 \text{ \AA}$, operated at 40 kV and 30 mA). XPS data was recorded on a Thermo Scientific K-Alpha instrument. ICP-OES spectroscopy measurements were conducted on an Agilent 5100 spectrometer. Nitrogen adsorption/desorption experiments were performed at 77.3 K on a Quantachrome ASiQwin instrument. X-ray absorption fine structure (XAFS) including X-ray absorption near-edge structure (XANES) and extended X-ray absorption fine structure (EXAFS) were collected at the SPring-8 14b2, where a pair of channel-cut Si (111) crystals was used in the monochromator.

Electrochemical measurements

Electrochemical measurements for HER were conducted on a CHI 760E instrument using a standard three-electrode configuration. A glassy carbon electrode coated with catalyst ink served as the working electrode. A Hg/HgO electrode was employed as the reference electrode, and a graphite rod was used as the counter electrode. The experiments were carried out in a thermostatically controlled water bath at 25 °C. For the preparation of the working electrode, 2.5 mg of the investigated catalyst and 5 μL of Nafion solution (20%) were mixed in a solvent mixture (240 μL , with a 3:1 v/v ratio of water to ethanol) and sonicated for 30 minutes to create a homogeneous dispersion. Subsequently, 5 μL of this catalyst ink was applied onto a glassy carbon electrode (GCE, 3 mm in diameter) and allowed to dry in the air.

Polarization curves were acquired at a scan rate of 5 mV s⁻¹ with 95% *iR*-compensation. Cyclic voltammetry (CV) was performed to determine the electrochemical double-layer capacitance within the potential range of 0.3 to 0.4 V *versus* RHE, with scan rates ranging from 10 to 120 mV s⁻¹. All measured potentials (*E*) were referenced

to the reversible hydrogen electrode (RHE) using the following equation:

$$E_{\text{RHE}} = E_{\text{Hg/HgO}} + 0.059 \text{PH} + E^0_{\text{Hg/HgO}}$$

Tafel slopes were determined by plotting the overpotential *vs.* the logarithm of current density ($\log |j|$). EIS was conducted in the frequency range from 10^5 Hz to 1 Hz with an amplitude of 5 mV at open circuit potential. The resistance of the solution (R_s) resulting from the Nyquist plot was used to correct the ohmic drop (iR -correction) for the HER measurement. All polarization curves were corrected with 95% iR compensation. The corrected potential could be obtained by $E_{\text{corrected}} = E_{\text{RHE}} - iR_s$. The stability of the catalysts was tested by means of chronopotentiometry ($V \sim t$) at a cathodic current density of 10 mA cm^{-2} . Note that before stability measurements, the catalyst underwent 200 CV cycles at a scan rate of 50 mV s^{-1} to active the catalyst.

Turnover frequency (TOF, s^{-1}) per metal site was calculated according to the following equation:

$$\text{TOF} = j / (n \times F \times N)$$

Where j is the geometric current density after 95% iR -correction, n is the number of electrons transferred in the reactions (2 for HER), F is the Faraday constant, and N is the molar number of active sites. Specifically, N was estimated via the total catalyst mass loading on the electrode (m , mg cm^{-2}), the weight percent of active metals in the catalysts (w , wt.%, determined by the ICP), and the molar mass (M , g mol^{-1}) according to the following equation:

$$N = m \times w / M$$

Mass activity (MA, A g^{-1}) was estimated via the catalyst loading (m , mg cm^{-2}) weight percent of the metal in the catalysts (w , wt.%) and the geometric current density (j , mA cm^{-2}) under a certain overpotential-based on the following equation:

$$\text{MA} = j / (m \times w)$$

The electrochemically active surface area (ECSA) value was calculated by integrating the hydrogen adsorption region with the following equation:

$$\text{ECSA} = \frac{Q_H / v}{0.21}$$

To obtain Q_H , CV is measured in the Ar-purged 1.0 M KOH between the potential range of 0-1 V *vs.* RHE at the scan rate of 50 mV s^{-1} . Q_H can be obtained by calculating the integral area of the hydrogen adsorption region of the CV. Here, v is the scan rate, and 0.21 mC cm^{-2} is the charge density transferred during the hydrogen adsorption for polycrystalline Pt.

Activation energy (E_a) calculation

To determine the E_a value, LSV curves were collected from -0.9 to -1.2 V *vs.* Hg/HgO at a scan rate of 10 mV s^{-1} in a 1.0 M KOH solution at various temperatures: 25, 30, 35, 40, 45, and 50 °C. Each reaction temperature

was maintained for 10 minutes to ensure temperature stability. For the heterogeneous HER, the exchange current density (j_0) can be represented using the Arrhenius equation:

$$j_0 = A e^{(\frac{E_a}{RT})}$$

Where A is an apparent pre-exponential factor, R is the ideal gas constant ($8.314 \text{ J}\cdot\text{K}^{-1}\text{mol}^{-1}$), and T is the temperature in Kelvin (K). Therefore, E_a can be further calculated by fitting the slope of the Arrhenius plot using the following equation:

$$\frac{\partial(\ln j_0)}{\partial(1/T)} = -\frac{E_a}{8.314}$$

AEMWE Test

The anion exchange membrane (AEM) electrolyzer employs a zero-gap cell configuration, consisting of a titanium alloy cell body for structural integrity and corrosion resistance, $1\times 1 \text{ cm}^2$ corrosion-resistant liquid flow chambers for anode/cathode compartments, nickel foam electrodes functioning as gas diffusion layers and catalyst supports, and Teflon gaskets to ensure hermetic sealing between membrane-electrode assemblies. The cathode ink was prepared by ultrasonication of a mixture of 10 mg catalyst and 30 μL Nafion solution (20%) in 2 mL solvent (1:1 v/v H₂O/ethanol) for 30 min. Prior to 12 h activation in 1 M KOH, cathodic catalysts (Co_n-Pt₁@N_{[5]/[6]}C and commercial Pt/C) were deposited on the KMem AM01 membrane (50 μm thickness) via airbrush spraying with controlled loading (2.5 mg cm^{-2}). The NiFe-LDH anode catalyst was electrodeposited in a three-electrode system (Ag/AgCl reference, Pt foil counter, Ni foam working electrode) using a -1.35 V(vs. Ag/AgCl) potential for 90 s in a 0.15 M Fe(NO₃)₃·9H₂O/Ni(NO₃)₂·6H₂O (3/2 molar ratio) solution, yielding uniform loading (3.0 mg cm^{-2}). The cathode and the anode were sandwiched with the membrane to form the AEM electrolyzer. AEMWE electrolyzer was operated at temperatures of 25-70 °C under ambient pressure, using 1 M KOH as the electrolyte. The performance of the AEMWE was evaluated by measuring the polarization curves from 1 V to 3 V at a scan rate of 50 mV/s. The stability of the AEMWE was conducted at a current density of 1 A·cm⁻² at 70 °C.

***In situ* surface-enhanced Raman spectroscopy measurements.**

In-situ Raman spectra were collected using a HORIBA LabRAM Soleil Raman microscope with a 532 nm excitation laser, while electrochemical curves were recorded using a CHI 760E electrochemical workstation. The solution was circulated by a pump to eliminate air bubble interference. The catalyst ink was prepared by dispersing catalyst (2.5 mg) into a mixture of ultrapure water (180 μL), ethanol (60 μL), and 20% Nafion (5 μL), followed by ultrasonic treatment for 30 minutes. Subsequently, 30 μL of the ink was applied to the surface of a glassy carbon electrode (GCE, diameter = 1 cm) in the in-situ cell and dried at 25 °C. To enhance the surface-enhanced Raman signal, a dispersion of Au nanoparticles was further applied to the modified electrode. A carbon rod served as the

counter electrode, and a Hg/HgO electrode was used as the reference electrode. Chronoamperometry was performed at various potentials in 1 M KOH during the Raman measurement.

Theoretical calculations

All density functional theory (DFT) calculations were done using the Vienna Ab initio Simulation Package (VASP).¹ The electron-ion interaction is described by the projector augmented wave method (PAW) with an energy cutoff of 525 eV for the plane-wave basis set.² The cell volume and atomic positions were optimized according to atomic forces with a threshold that the calculated force on each atom is smaller than 0.02 eV/Å. As for the exchange-correlation functional, the generalized gradient approximation (GGA) of Perdew-Burke-Ernzerhof (PBE) is used.³ The Grimme's dispersion correction with Becke-Johnson damping (DFT-D3BJ) is included.^{4, 5} A 3×3×1 Γ-centered Monkhorst-Pack k-point mesh is adopted for all calculations. The k-points mesh is increased to 6×6×1 for calculating the density of states (DOS). The atomic charge was determined by performing Bader charge analysis.⁶ The N atoms were doped into an 8×8×1 graphene supercell with a 25 Å vacuum slab along the z-direction. The loaded Co₂₅ cluster was built by the atomic simulation environment (ASE).⁷ The Pt₁ binding energy ($E_b[\text{Pt}_1]$) is defined as:

$$E_b[\text{Pt}_1] = E[\text{substrate} + \text{Pt}_1] - E[\text{substrate}] - E[\text{Pt}_{\text{bulk}}]$$

where $E[\text{substrate} + \text{Pt}_1]$ is the energy of Pt₁ loaded substrate, $E[\text{substrate}]$ is the energy of the bare substrate, and $E[\text{Pt}_{\text{bulk}}]$ is the energy of bulk Pt (per Pt atom). Transition states are determined by climb image nudged elastic band (CI-NEB) calculations to investigate the H–O bond breaking barrier for H₂O*.⁸ Gibbs free energies (G) of all gaseous and absorbed surface species are evaluated at $T=298.15$ K, by taking the zero-point energy and entropy contribution into account:

$$G = E_0 + \text{ZPE} + \Delta U_{0 \rightarrow T} + TS$$

where E_0 is the electronic energy, ZPE is the zero-point energy, $\Delta U_{0 \rightarrow T}$ is the internal energy contribution, and S is the entropy contribution. $\Delta U_{0 \rightarrow T}$ and S are calculated by considering the contributions from translation, rotational motion, vibrational motion, and electronic motion. The corresponding partition function was used to calculate the entropy contribution⁹ and the post-analysis is done by using VASPKIT.¹⁰ The HER free energy diagram was investigated by considering the following critical steps:

1. *+H₂O→H₂O*(water adsorption)
2. H₂O*→H*+OH*(water dissociation)
3. OH*+e⁻→OH⁻(OH desorption)
4. H*→½H₂(hydrogen evolution)

The free energy of OH⁻ is evaluated as ¹¹:

$$\Delta G_{(\text{OH}^-)} = \frac{1}{2} [G_{(2^* + \text{H}_2 + 2\text{OH}^-)} - G_{(2\text{OH}^*)} - G_{(\text{H}_2)}] = \frac{1}{2} [G_{(2^* + 2\text{H}_2\text{O})} - G_{(2\text{OH}^*)} - G_{(\text{H}_2)}]$$

The ΔG_{H^*} map on the surface of the catalyst (**Fig. 6e**) is done by employing rigid scan. Single H atom is placed on the van der Waals surface of the substrate, with the substrate kept fixed. Only the z-coordinate of the H atom is relaxed during the calculation. The surface of the substrate was sampled by calculating ~750 nearly equally spaced H adsorption sites. Only Γ point is used in VASP during the rigid scan. The free energy ΔG_{H^*} of a certain site was determined as

$$\Delta G_{\text{H}^*} = E_{0,\text{H}^*} - E_{0,*} - \frac{1}{2} E_{0,\text{H}_2} + 0.24 \text{ eV}$$

by assuming the zero-point energy and entropy change is 0.24 eV.¹²

Synthesis of ZIF-8@ZIF-67

In a typical preparation, Zn(NO₃)₂·6H₂O (5.95 g) and 2-methylimidazole (6.16 g) were separately dissolved in 150 mL of methanol. The two solutions were then mixed and stirred at room temperature for 24 h to form white ZIF-8 precipitates. The precipitates were collected by centrifugation, washed with methanol, and dried under vacuum at 60 °C overnight. Next, 0.004 mol of ZIF-8 was dispersed in 200 mL of methanol. Co(NO₃)₂·6H₂O (465.6 mg) and 2-methylimidazole (492.6 mg) were dissolved in 8 mL of methanol. The Co(NO₃)₂·6H₂O solution was added to the ZIF-8 dispersion, followed by the 2-methylimidazole solution. The mixture was stirred at room temperature for 24 h, resulting in the formation of light purple precipitates. These precipitates were isolated by centrifugation, washed with methanol and ethanol, and dried under vacuum at 60 °C overnight to yield the purified final product.

Synthesis of Co_n@N_[6]C

ZIF-8@ZIF-67 was annealed at 920 °C for 3 hours in Ar at a rate of 2 °C·min⁻¹, and the product was washed with a 0.85 M H₂SO₄ solution at room temperature for 12 h. The product was centrifugally washed with ultrapure water several times and vacuum dried at 60 °C overnight, denoted as Co_n@N_[6]C.

Synthesis of Co_n@N_{[5]/[6]}C

The synthetic procedure for Co_n@N_{[5]/[6]}C is similar to that of Co_n@N_[6]C, with the primary difference being the pyrolysis atmosphere, which is changed from Ar to 5 mol% H₂/Ar.

Synthesis of Co_n-Pt_I@N_{[5]/[6]}C and Co_n-Pt_I@N_[6]C

The as-prepared Co_n@N_{[5]/[6]}C (30 mg) was dispersed in 10 mL of ultrapure water for 30 minutes. Subsequently, 300 μL of H₂PtCl₆·6H₂O solution (20 mg/mL) was introduced. After further ultrasonication for 30 minutes, the mixture was stirred at 60 °C for 16.5 h, and the suspension was separated by centrifugation. The product was washed with ultrapure water, vacuum-dried at 60 °C overnight, and designated as Co_n-Pt_I@N_{[5]/[6]}C.

The synthesis of $\text{Co}_n\text{-Pt}_1@\text{N}_{[6]}\text{C}$ is similar to $\text{Co}_n\text{-Pt}_1@\text{N}_{[5]/[6]}\text{C}$, with the only difference being the use of $\text{Co}_n@\text{N}_{[6]}\text{C}$ instead of $\text{Co}_n@\text{N}_{[5]/[6]}\text{C}$. The Pt contents in $\text{Co}_n@\text{N}_{[5]/[6]}\text{C}$ and $\text{Co}_n@\text{N}_{[6]}\text{C}$ determined by inductively coupled plasma mass spectrometry (ICP-MS) are 8.38 wt.% and 8.52%, respectively.

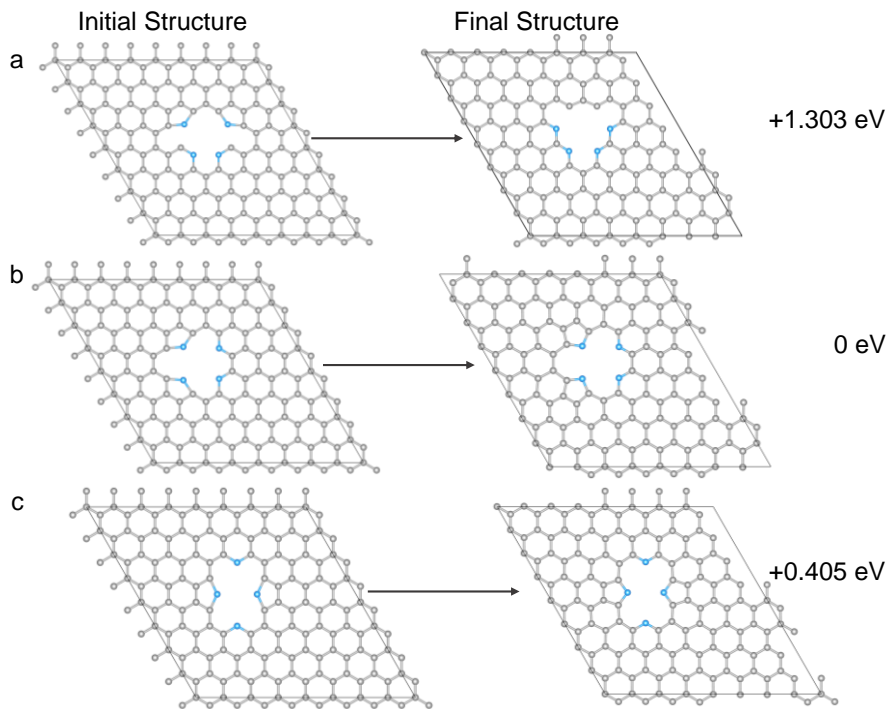


Fig. S1. Three possible initial structures of N_{[5]/[6]}C configurations are depicted alongside their corresponding DFT optimized structural models, with the relative electronic energies of the DFT optimized structures provided.

Among these configurations, the relative electronic energies of the DFT optimized structures for configurations a and c are both higher than those for configuration b, indicating that configuration b is the most stable.

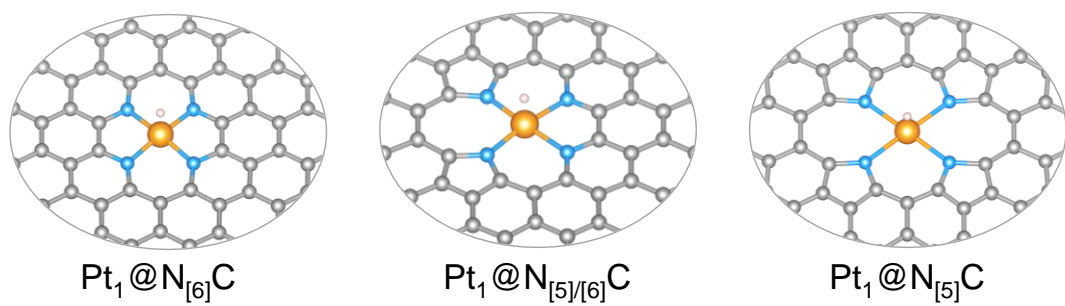


Fig. S2. Optimized H* adsorption structures of Pt₁@N_[6]C, Pt₁@N_{[5]/[6]}C, and Pt₁@N_[5]C.

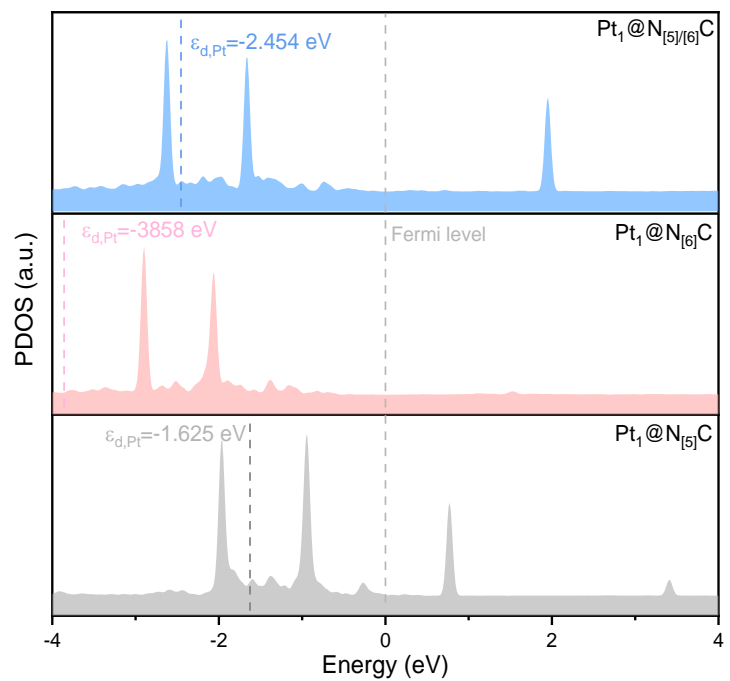


Fig. S3. Calculated PDOS of Pt 5d for $\text{Pt}_1@\text{N}_{[6]}\text{C}$, $\text{Pt}_1@\text{N}_{[5]/[6]}\text{C}$, and $\text{Pt}_1@\text{N}_{[5]}\text{C}$.

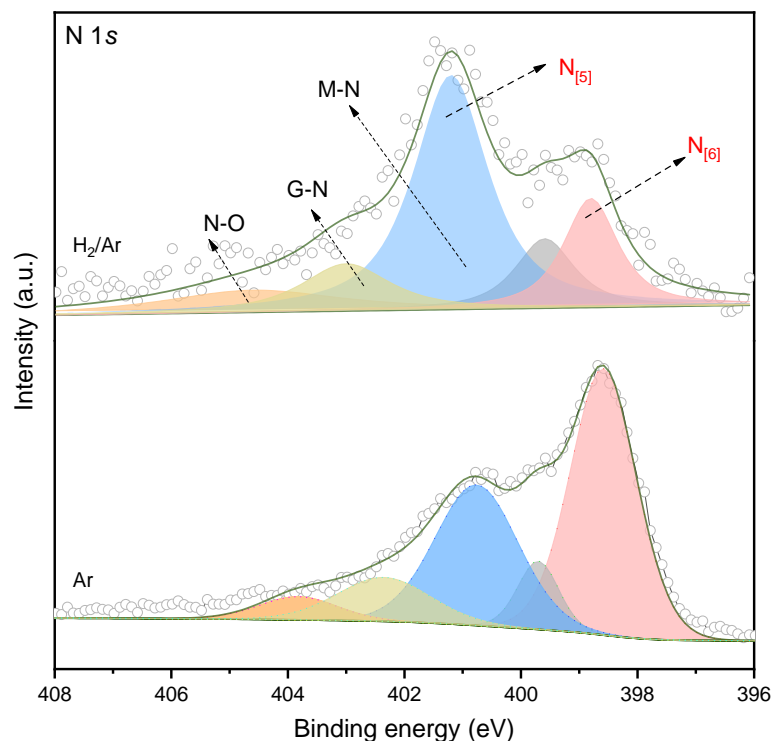


Fig. S4. High-resolution XPS N 1s spectra of ZIF-67 pyrolysis products in H_2/Ar and Ar.

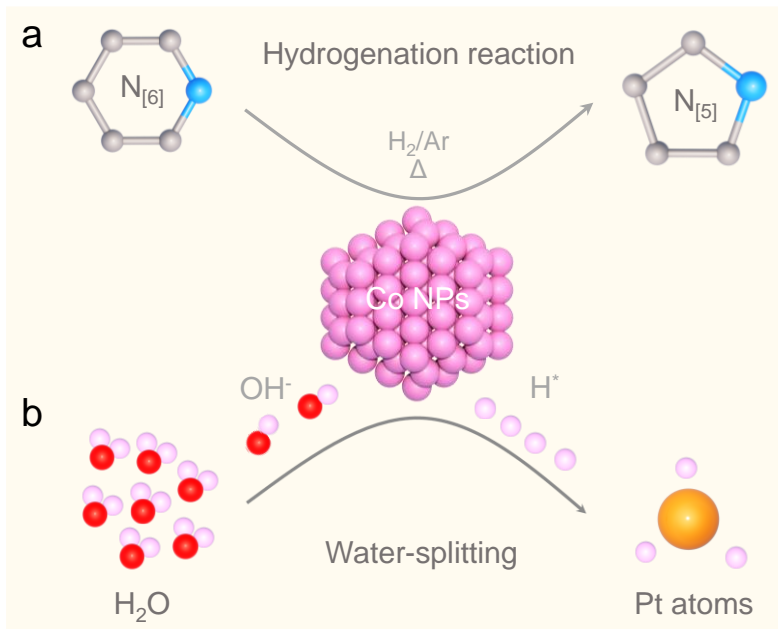


Fig. S5. The function of Co_n : (a) Catalyzing hydrogenation reaction; (b) Severing as OH^* adsorption site

As depicted in **Fig. S6**, Co_n serves dual functions: 1) It can cause the transformation of $\text{N}_{[6]}$ to $\text{N}_{[5]}$ through hydrogenation ($\text{Co} + \text{C} + 2\text{H}_2 \rightarrow \text{Co} + \text{CH}_4$), regulating the content of $\text{N}_{[5]}$ and $\text{N}_{[6]}$ to 1/1. 2) It can effectively adsorb OH^* from H_2O to supply H^* to Pt_1 .

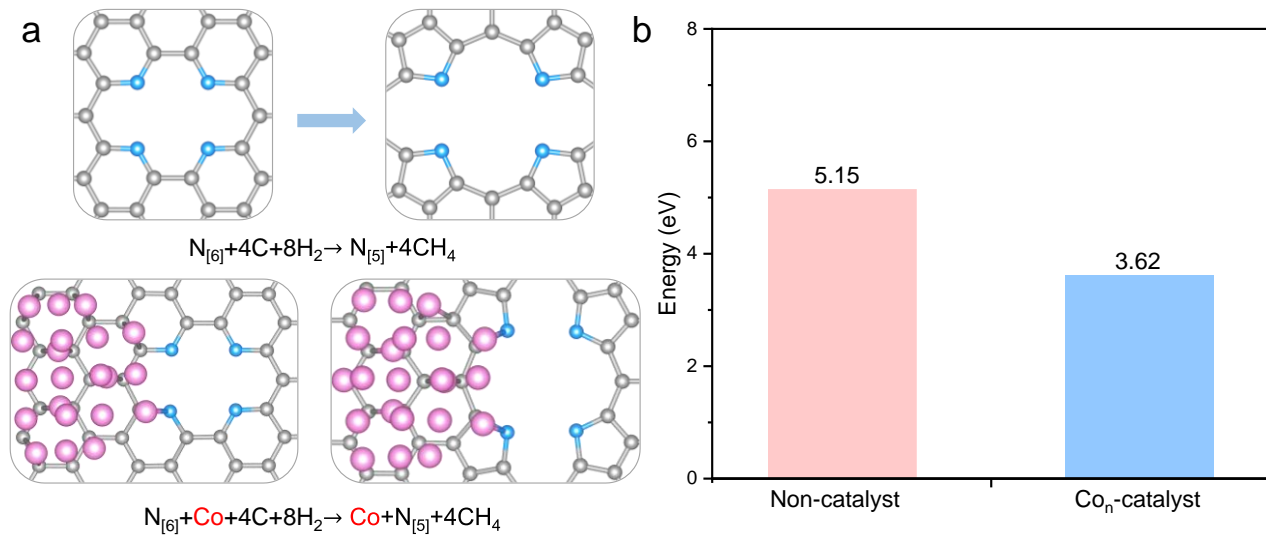


Fig. S6. (a) Schematic models and (b) reaction energy barrier of Co_n -incorporated vs. Co-free systems.

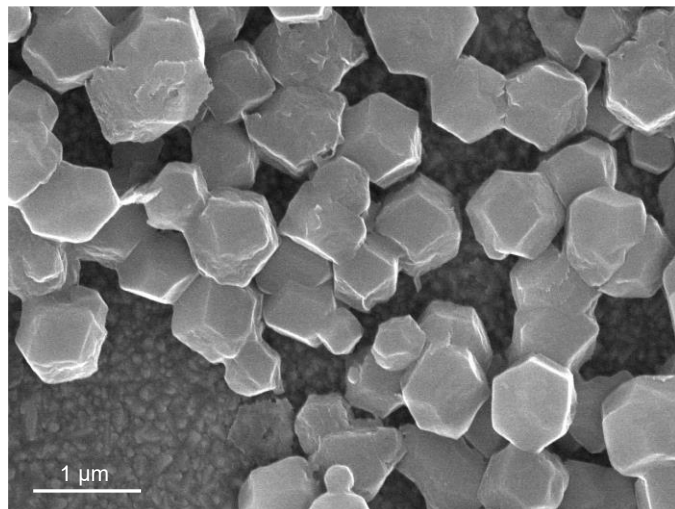


Fig. S7. SEM image of core-shell ZIF-8@ZIF-67.

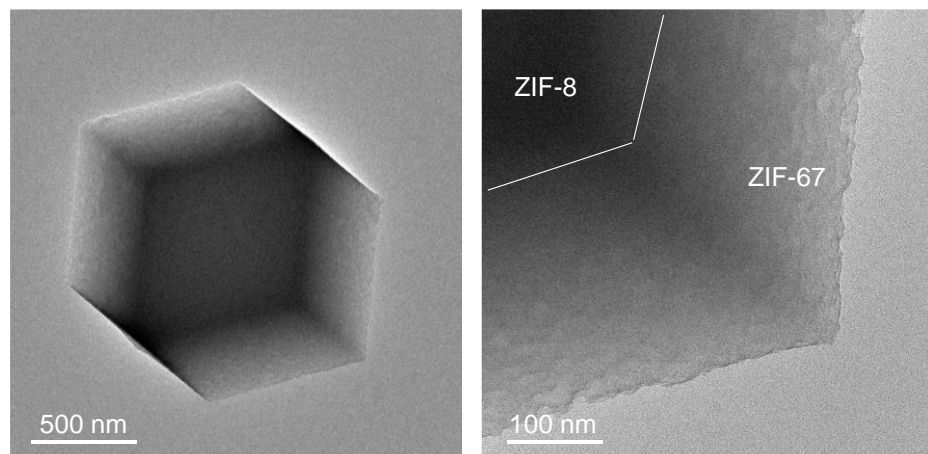


Fig. S8. TEM images of core-shell ZIF-8@ZIF-67.

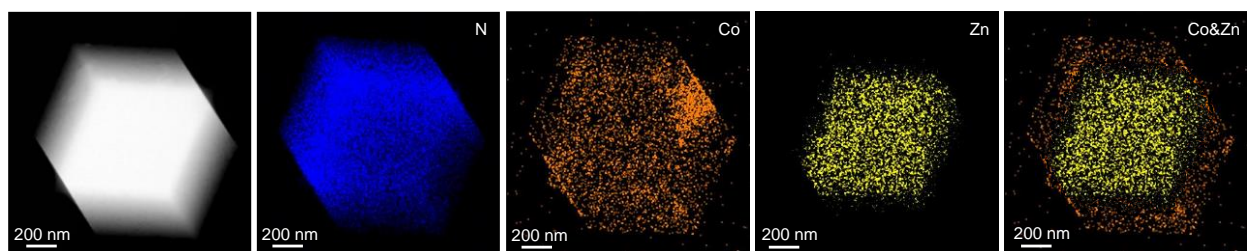


Fig. S9. STEM image and energy-dispersive X-ray spectroscopy (EDS) element mapping of core-shell ZIF-8@ZIF-67.

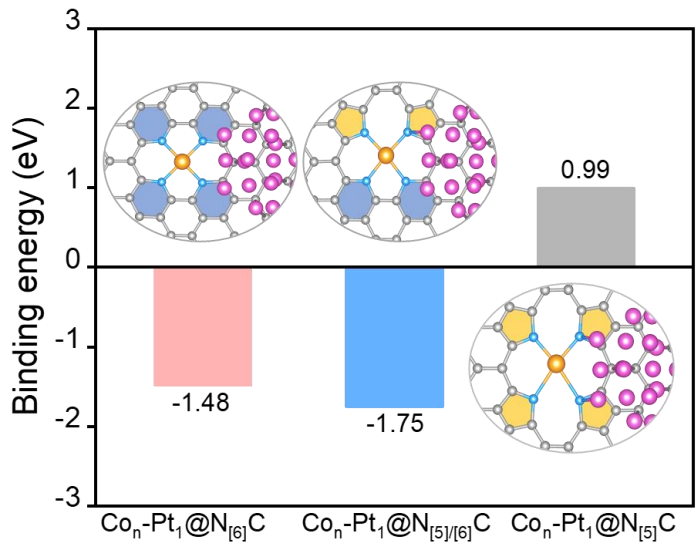


Fig. S10. Binding energies between $\text{Co}_n\text{-N}_{[5]/[6]}\text{C}$, $\text{Co}_n\text{-N}_{[6]}\text{C}$, and $\text{Co}_n\text{-N}_{[5]}\text{C}$ and Pt (Inset: Structure models of $\text{Co}_n\text{-Pt}_1@\text{N}_{[5]/[6]}\text{C}$, $\text{Co}_n\text{-Pt}_1@\text{N}_{[6]}\text{C}$, and $\text{Co}_n\text{-Pt}_1@\text{N}_{[5]}\text{C}$). Note that $\text{Co}_n\text{-N}_{[5]}\text{C}$ exhibits positive binding energy towards Pt_1 , suggesting the poor stability of $\text{Co}_n\text{-Pt}_1@\text{N}_{[5]}\text{C}$.

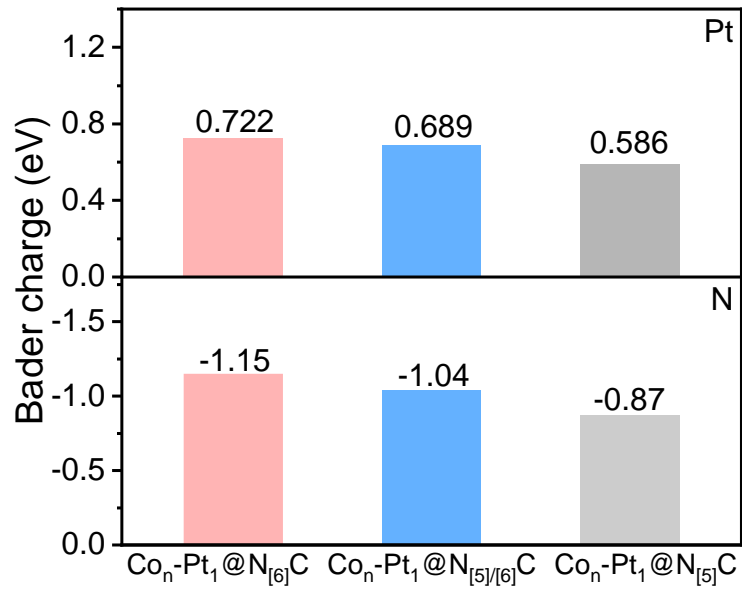


Fig. S11. Bader charge of Pt and N in $\text{Co}_n\text{-Pt}_1@\text{N}_{[5]/[6]}\text{C}$, $\text{Co}_n\text{-Pt}_1@\text{N}_{[6]}\text{C}$, and $\text{Co}_n\text{-Pt}_1@\text{N}_{[5]}\text{C}$.

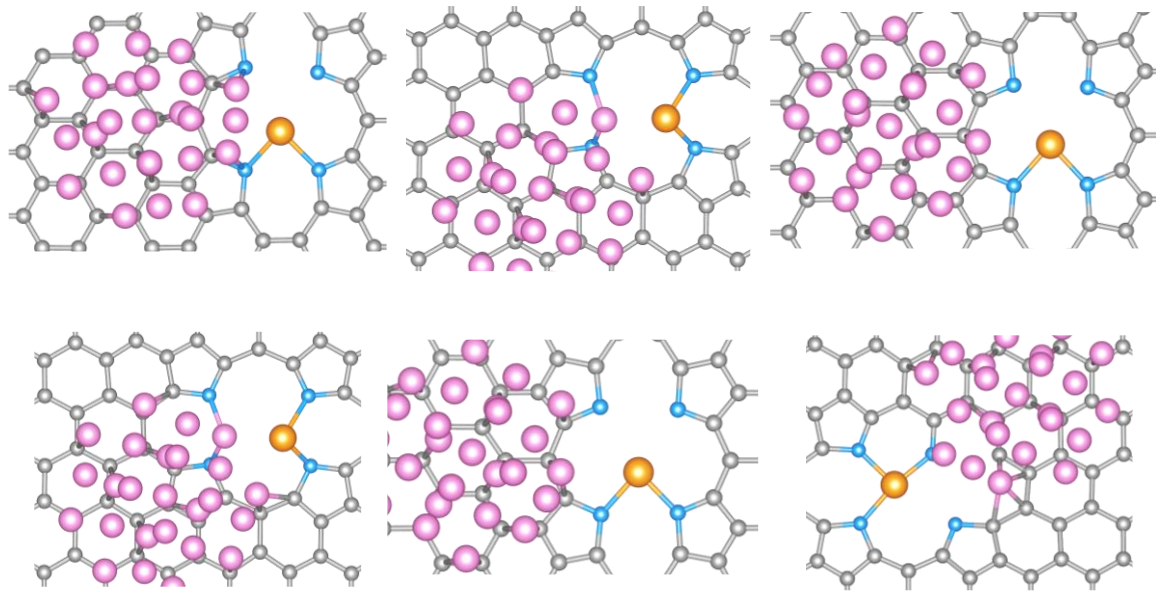


Fig. S12. Screening process for $\text{Co}_n\text{-Pt}_1\text{@N}_{[5]} \text{C}$ models by DFT.

As exhibited in **Fig. S12**, when introducing Co to the $\text{N}_{[5]} \text{C}$ model, the interference from some Co atoms makes it extremely difficult for Pt_1 to coordinate with four $\text{N}_{[5]}$.

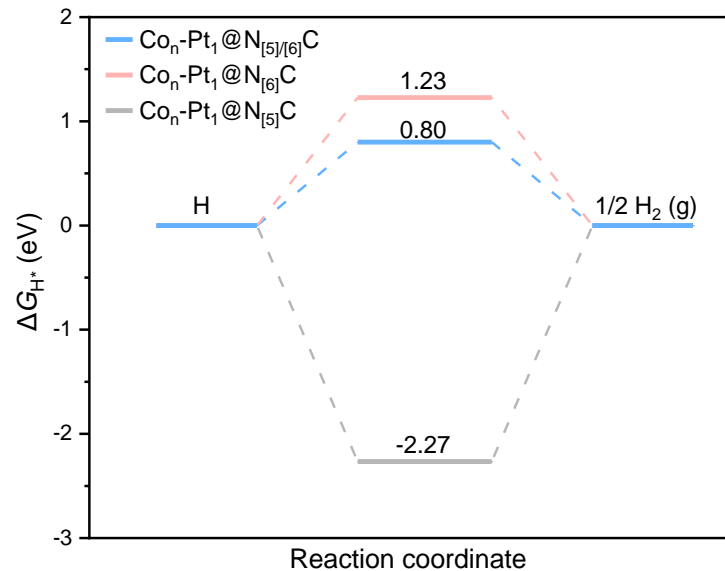


Fig. S13. Gibbs free energy of H^* adsorption on $\text{Co}_n\text{-Pt}_1\text{@N}_{[5]/[6]} \text{C}$, $\text{Co}_n\text{-Pt}_1\text{@N}_{[6]} \text{C}$, and $\text{Co}_n\text{-Pt}_1\text{@N}_{[5]} \text{C}$.

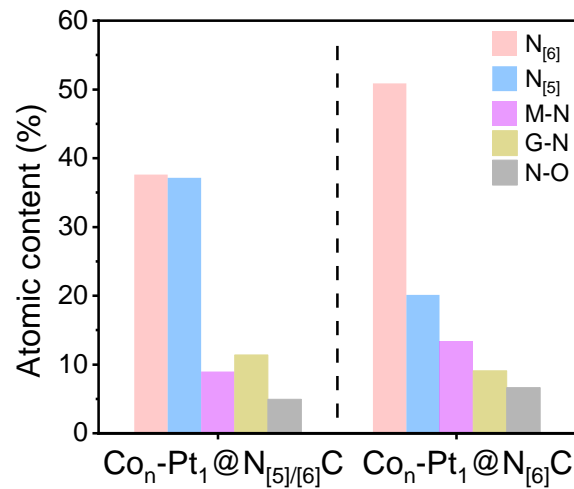


Fig. S14. Corresponding contents of N₆, N₅, M-N, G-N, and O-N in Co_n-Pt₁@N_{5/[6]}C and Co_n-Pt₁@N₆C.

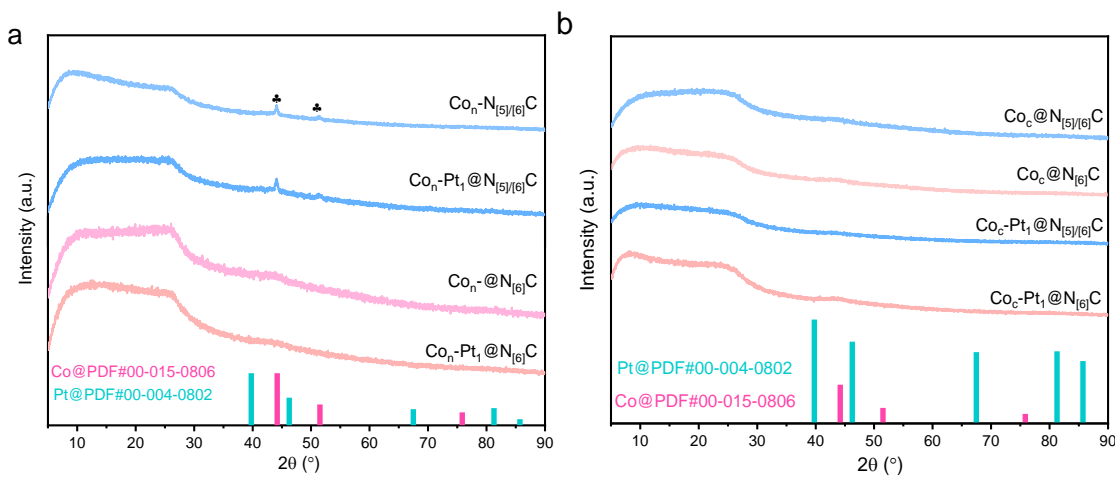


Fig. S15. XRD pattern of (a) Co_n-N_{5/[6]}C, Co_n-N₆C, Co_n-Pt₁@N_{5/[6]}C, and Co_n-Pt₁@N₆C; and (b) Co_c-N_{5/[6]}C, Co_c-N₆C, Co_c-Pt₁@N_{5/[6]}C, and Co_c-Pt₁@N₆C.

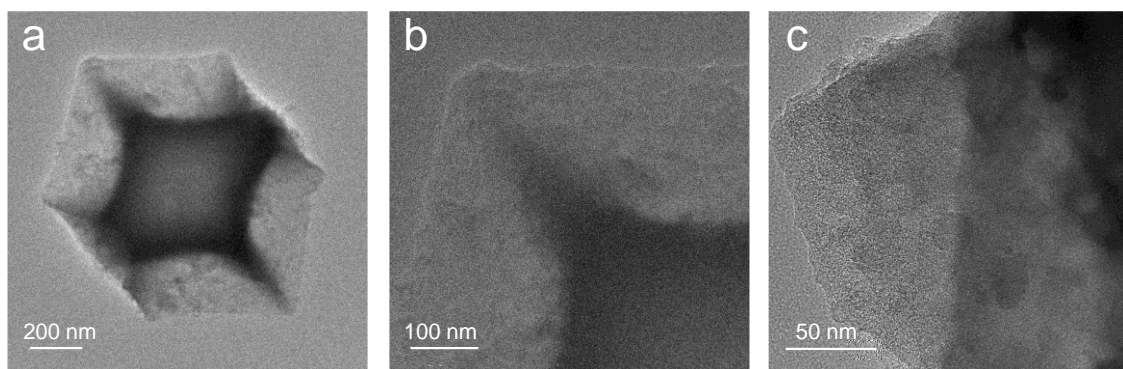


Fig. S16. TEM images of Co_c-Pt₁@N_{5/[6]}C.

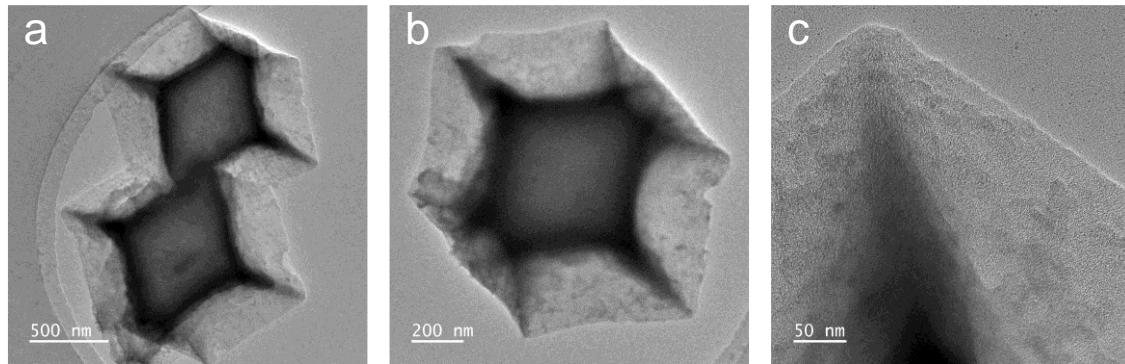


Fig. S17. TEM images of $\text{Co}_c\text{-Pt}_1\text{@N}_{[6]}\text{C}$.

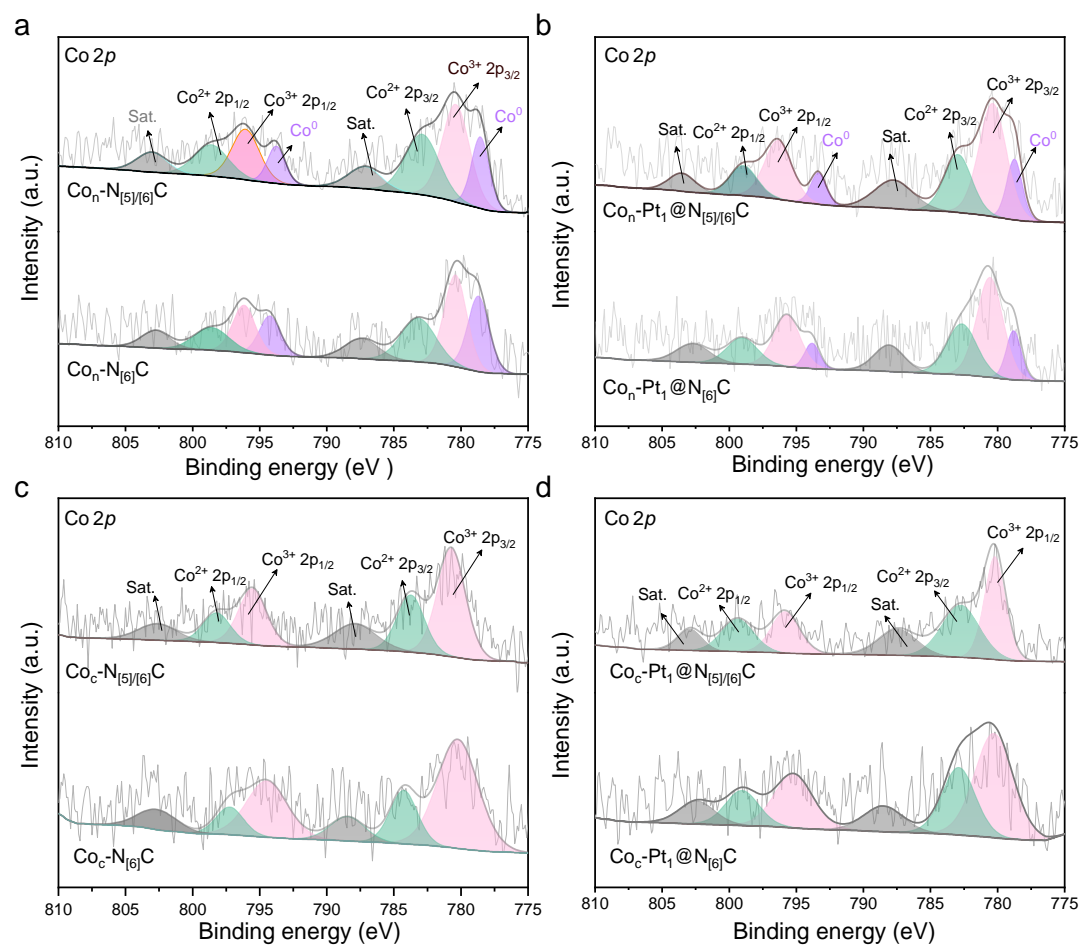


Fig. S18. High-resolution XPS spectra of Co 2p for (a) $\text{Co}_n\text{-N}_{[5]/[6]}\text{C}$ and $\text{Co}_n\text{-N}_{[6]}\text{C}$, (b) High-resolution XPS spectra of Co 2p $\text{Co}_n\text{-Pt}_1\text{@N}_{[5]/[6]}\text{C}$ and $\text{Co}_n\text{-Pt}_1\text{@N}_{[6]}\text{C}$, (c) $\text{Co}_c\text{-N}_{[5]/[6]}\text{C}$ and $\text{Co}_c\text{-N}_{[6]}\text{C}$, (d) $\text{Co}_c\text{-Pt}_1\text{@N}_{[5]/[6]}\text{C}$ and $\text{Co}_c\text{-Pt}_1\text{@N}_{[6]}\text{C}$.

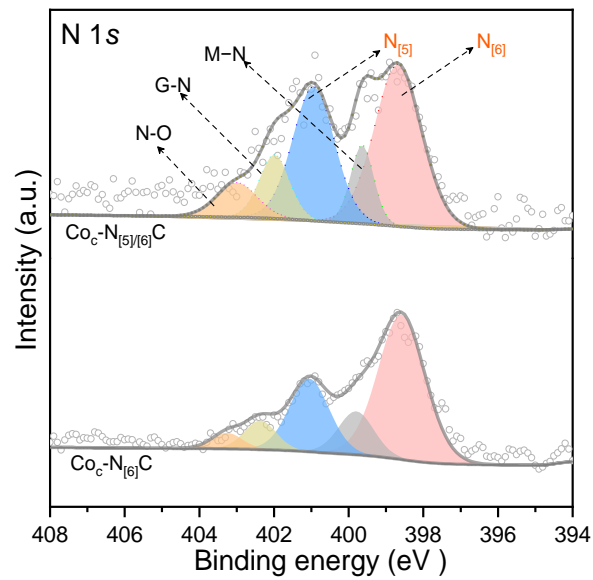


Fig. S19. XPS spectra of N 1s for $\text{Co}_c\text{-N}_{[5]/[6]}\text{C}$ and $\text{Co}_c\text{-N}_{[6]}\text{C}$.

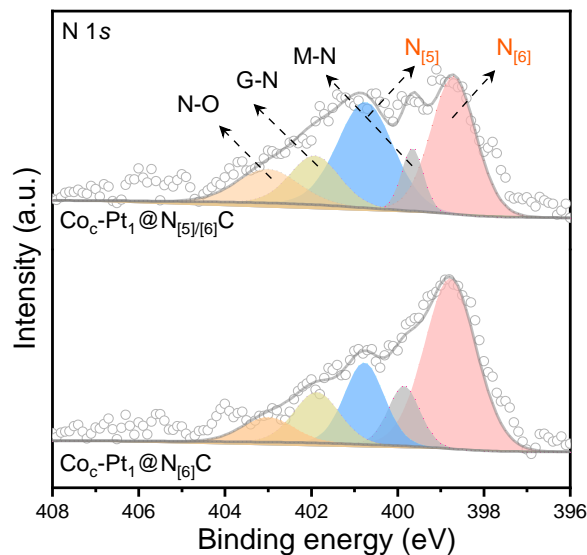


Fig. S20. XPS spectra of N 1s for $\text{Co}_c\text{-Pt}_1@\text{N}_{[5]/[6]}\text{C}$ and $\text{Co}_c\text{-Pt}_1@\text{N}_{[6]}\text{C}$.

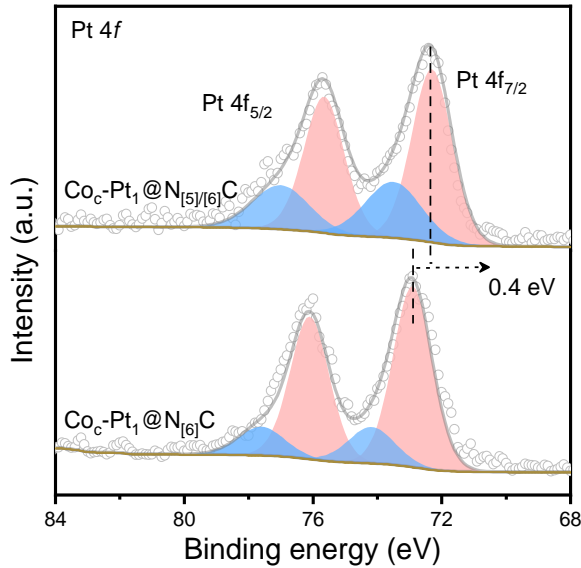


Fig. S21. High-resolution XPS spectra of Pt 4f.

The XRD patterns of $\text{Co}_n\text{-N}_{[5]/[6]}\text{C}$ and $\text{Co}_n\text{-Pt}_1@\text{N}_{[5]/[6]}\text{C}$ exhibit diffraction peaks at 44.22° and 51.52° , corresponding to the (1 1 1) and (2 0 0) crystal planes of Co_n , respectively (**Fig. S15a**). Notably, $\text{Co}_n\text{-N}_{[6]}\text{C}$ and $\text{Co}_n\text{-Pt}_1@\text{N}_{[6]}\text{C}$ prepared in Ar exhibit weaker diffraction peaks of Co_n , which may be due to the lack of H_2 participation, thereby limiting the ring-reconstruction reaction and preventing significant collapse of the internal structure. As a result, the Co_n appear to be more tightly encapsulated by the carbon layers, as evidenced by the aberration-corrected STEM images (**Fig. 3g**). When the Co content is reduced, $\text{N}_{[5]/[6]}\text{C}$ and $\text{N}_{[6]}\text{C}$ loaded with Co atoms or clusters were obtained (named $\text{Co}_c\text{-N}_{[5]/[6]}\text{C}$ and $\text{Co}_c\text{-N}_{[6]}\text{C}$). **Fig. S15b** suggests that Co may exist in the form of atoms or clusters, as confirmed by the XPS spectra of Co (**Fig. S18c-d**). Indeed, no significant nanoparticles were observed in the TEM images (**Fig. S16-17**). From **Fig. S19-20**, it is evident that reducing the amount of Co results in the $\text{N}_{[5]}/\text{N}_{[6]}$ atomic ratio remaining almost 1/1, with a slight decrease in the percentage of $\text{N}_{[5]}$. This may be due to the relatively weaker catalytic effect caused by the lower Co content, indicating that ring reconstruction cannot occur without the participation of Co. Furthermore, the XRD patterns of both systems show no crystal diffraction peaks of Pt, confirming that all Pt exists in the form of atoms, as evidenced by the XPS spectra of Pt (**Fig. S21**).

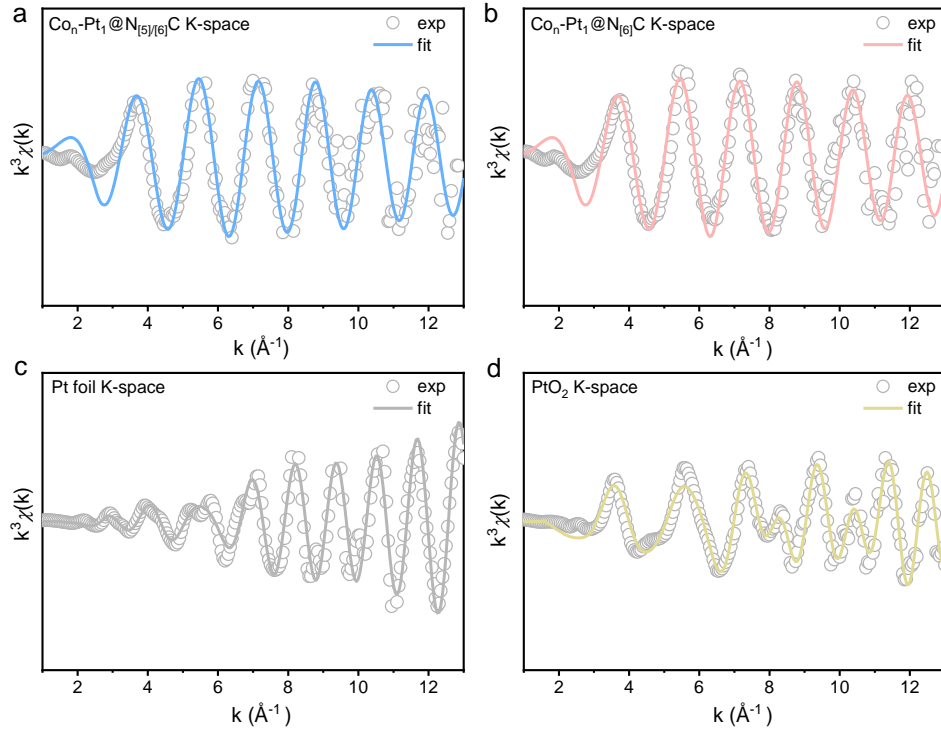


Fig. S22. Fourier-transformed magnitude of Pt L₃ EXAFS spectra in K space, (a) Co_n-Pt₁@N_{[5][6]}C, (b) Co_n-Pt₁@N_[6]C, (c) Pt foil, (d) PtO₂.

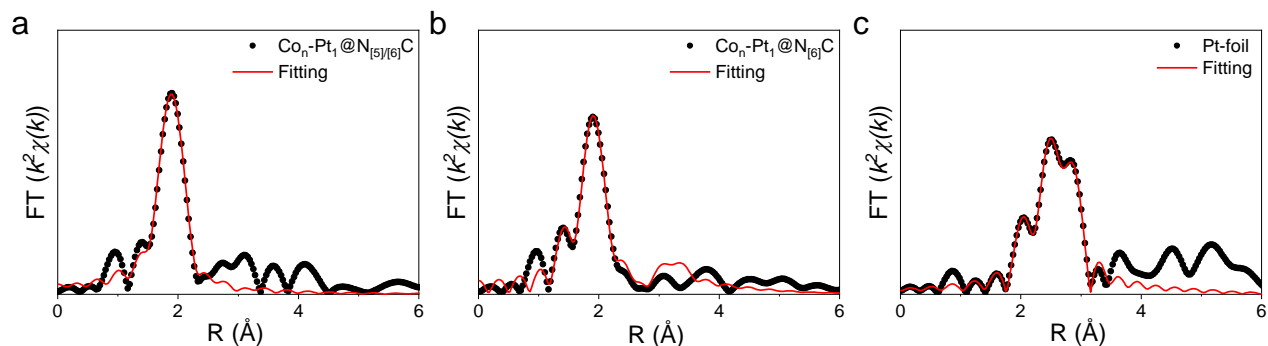


Fig. S23. Fourier-transformed magnitude of Pt L₃ EXAFS spectra in R space. (a) Co_n-Pt₁@N_{[5][6]}C, (b) Co_n-Pt₁@N_[6]C, (c) Pt foil.

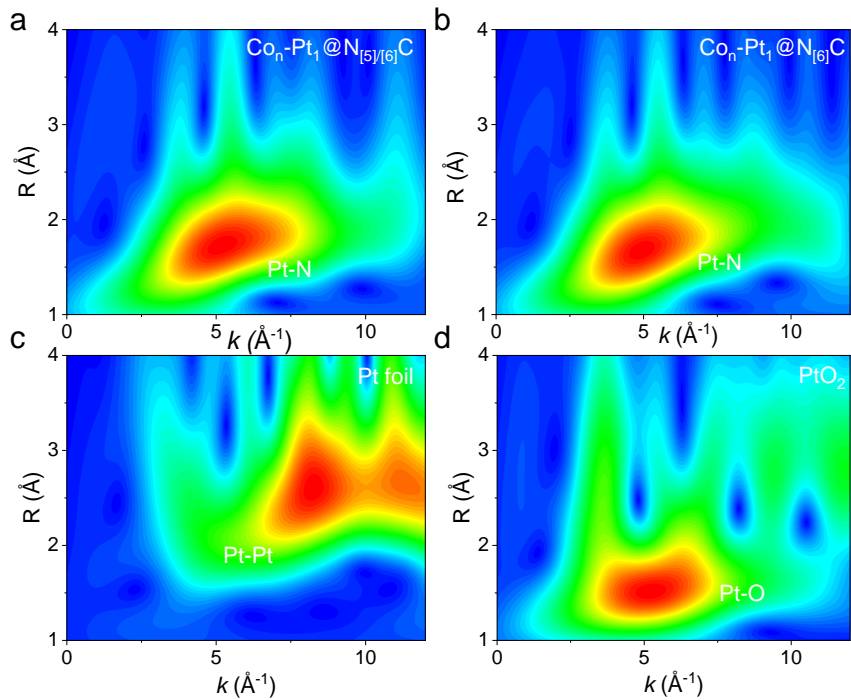


Fig. S24. (a) wavelet-transformed k^2 -weighted EXAFS spectra of $\text{Co}_n\text{-Pt}_1@\text{N}_{[5]/[6]}\text{C}$, (b) $\text{Co}_n\text{-Pt}_1@\text{N}_{[6]}\text{C}$, (c) Pt foil, and (d) PtO_2 .

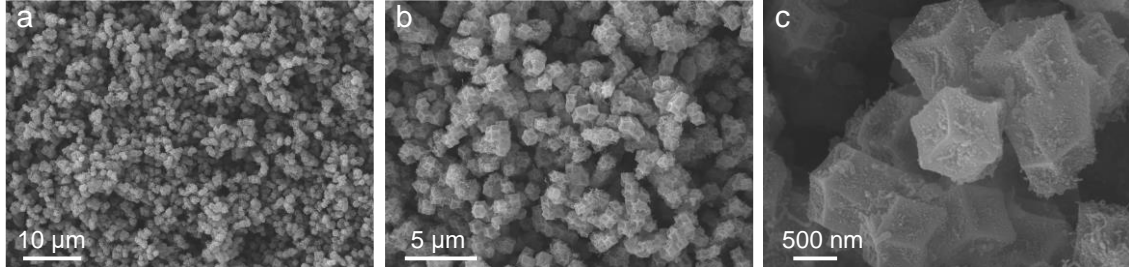


Fig. S25. SEM images of $\text{Co}_n\text{-N}_{[5]/[6]}\text{C}$.

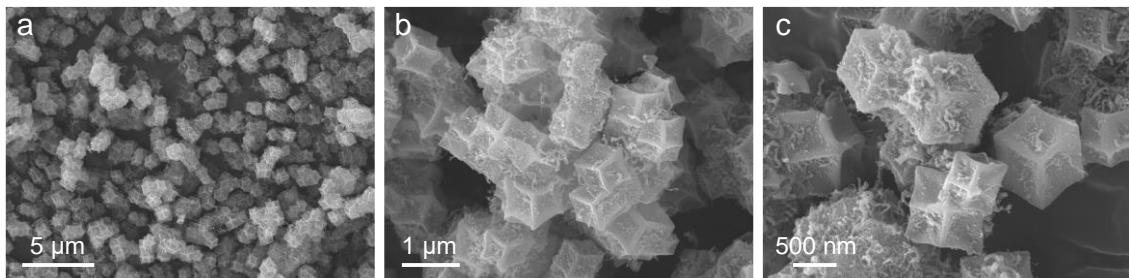


Fig. S26. SEM images of $\text{Co}_n\text{-N}_{[6]}\text{C}$.

Note that regardless of whether H_2 is present or not, the materials after pyrolysis are densely covered with carbon nanotubes (CNTs). This may be attributed to the fact that the evaporation of Zn at high pyrolysis temperatures plays a similar role to H_2 in promoting the rapid formation of Co, which catalyzes the growth of CNTs.^{13,14}

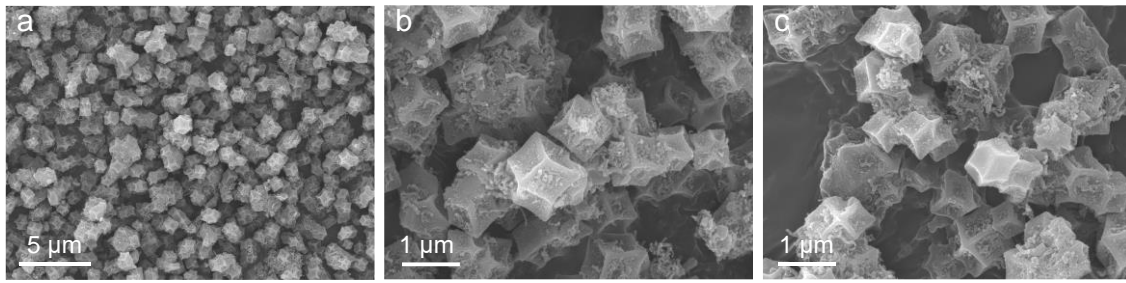


Fig. S27. SEM images of $\text{Co}_n\text{-Pt}_l@\text{N}_{[5]/[6]}\text{C}$.

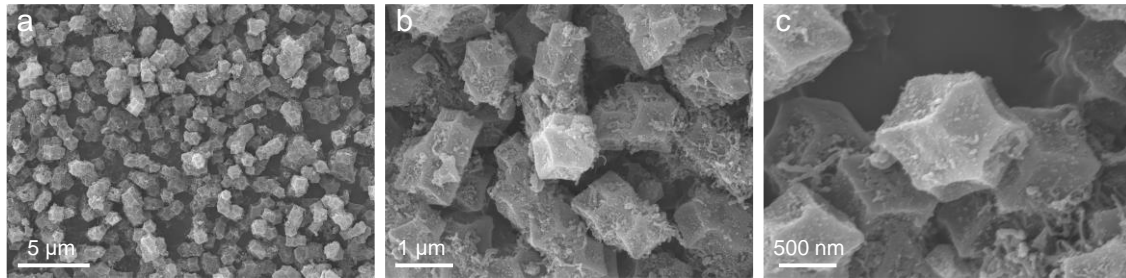


Fig. S28. SEM images of $\text{Co}_n\text{-Pt}_l@\text{N}_{[6]}\text{C}$.

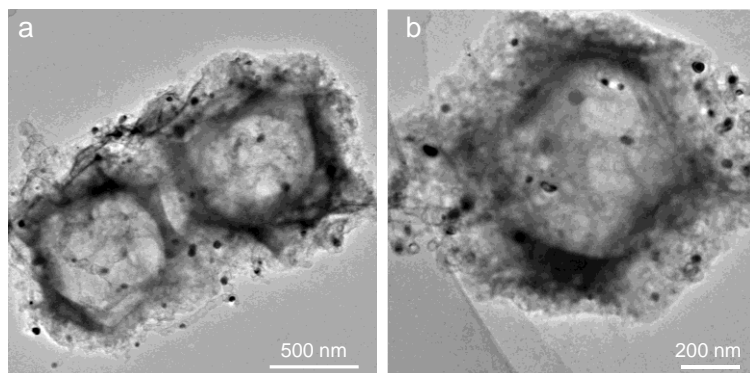


Fig. S29. TEM images of $\text{Co}_n\text{-N}_{[5]/[6]}\text{C}$.

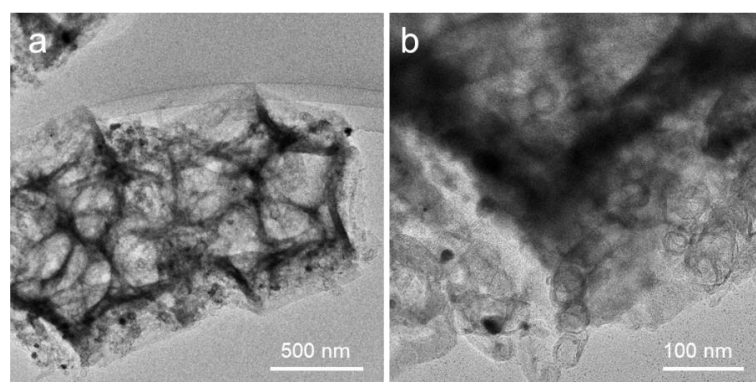


Fig. S30. TEM images of $\text{Co}_n\text{-N}_{[6]}\text{C}$. The internal structure did not undergo significant collapse, indicating that the Co_n may be encapsulated by the carbon layers.

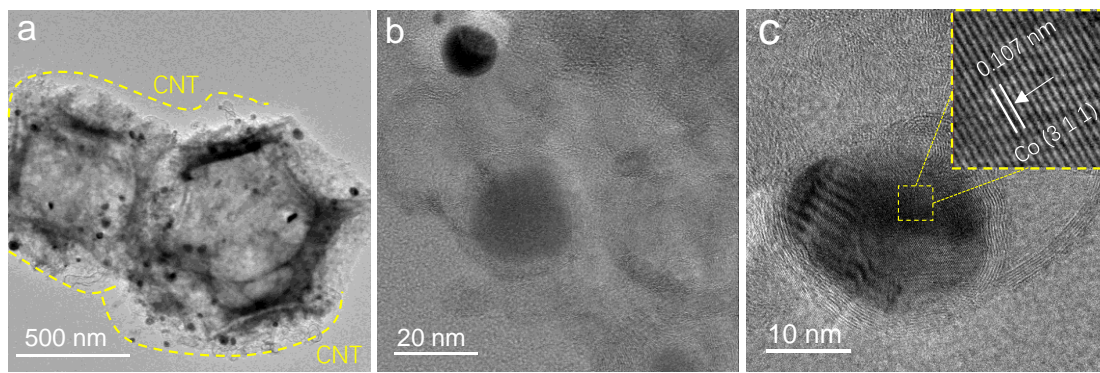


Fig. S31. TEM images of $\text{Co}_n\text{-Pt}_1@\text{N}_{[5]/[6]} \text{C}$.

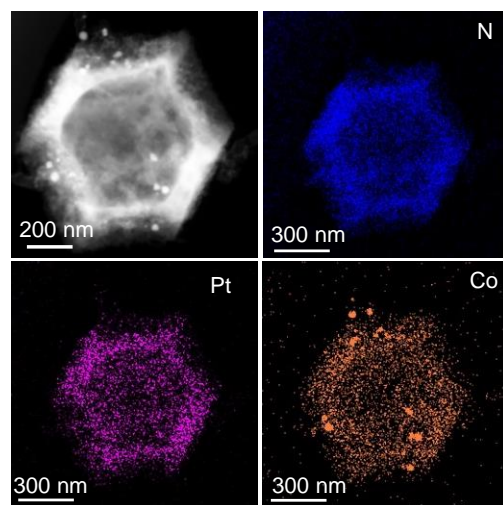


Fig. S32. STEM images and EDS mapping of $\text{Co}_n\text{-Pt}_1@\text{N}_{[5]/[6]} \text{C}$.

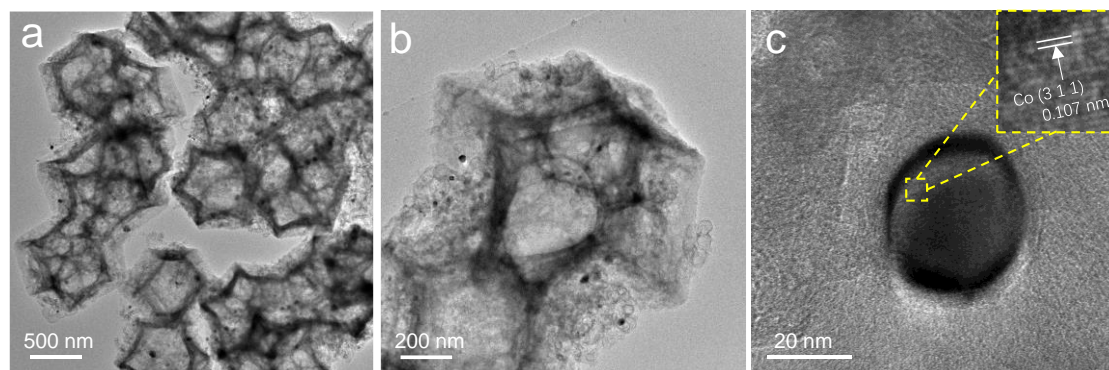


Fig. S33. TEM (a, b) and HRTEM (c) images of $\text{Co}_n\text{-Pt}_1@\text{N}_{[6]} \text{C}$.

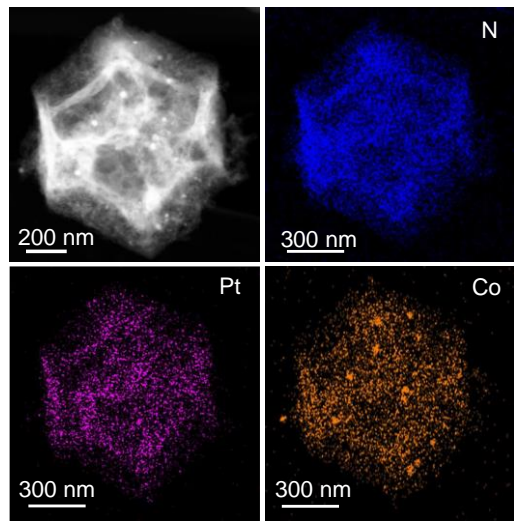


Fig. S34. STEM images and EDS mapping of $\text{Co}_n\text{-Pt}_1@\text{N}_{[6]}\text{C}$.

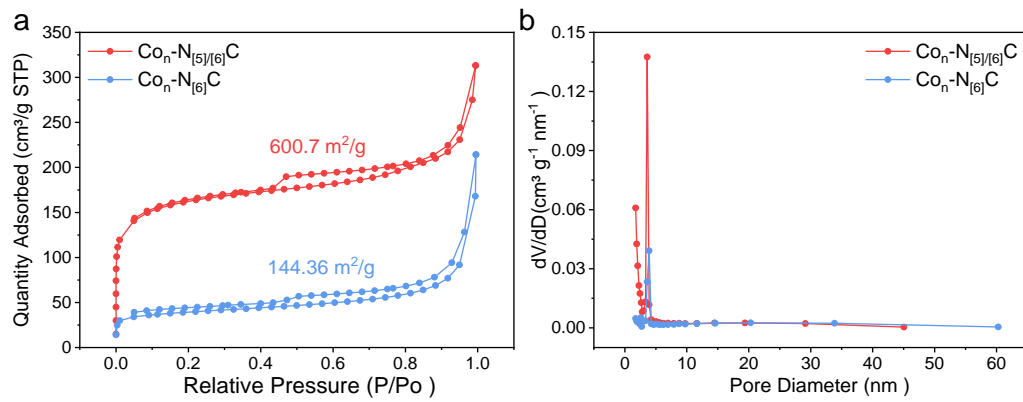


Fig. S35. (a) N_2 adsorption-desorption isotherm curves and (b) corresponding pore distributions of $\text{Co}_n\text{-N}_{[5]/[6]}\text{C}$ and $\text{Co}_n\text{-N}_{[6]}\text{C}$.

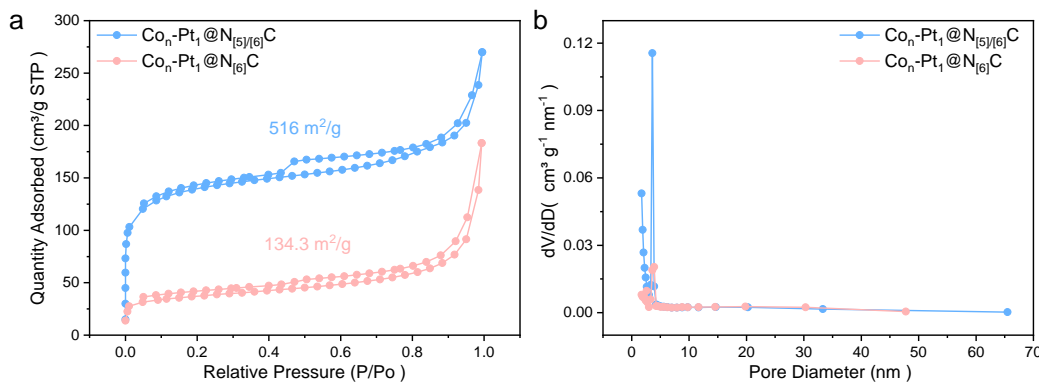


Fig. S36. (a) N_2 adsorption-desorption isotherm curves and (b) corresponding pore distributions of $\text{Co}_n\text{-Pt}_1\text{-N}_{[5]/[6]}\text{C}$ and $\text{Co}_n\text{-Pt}_1\text{-N}_{[6]}\text{C}$.

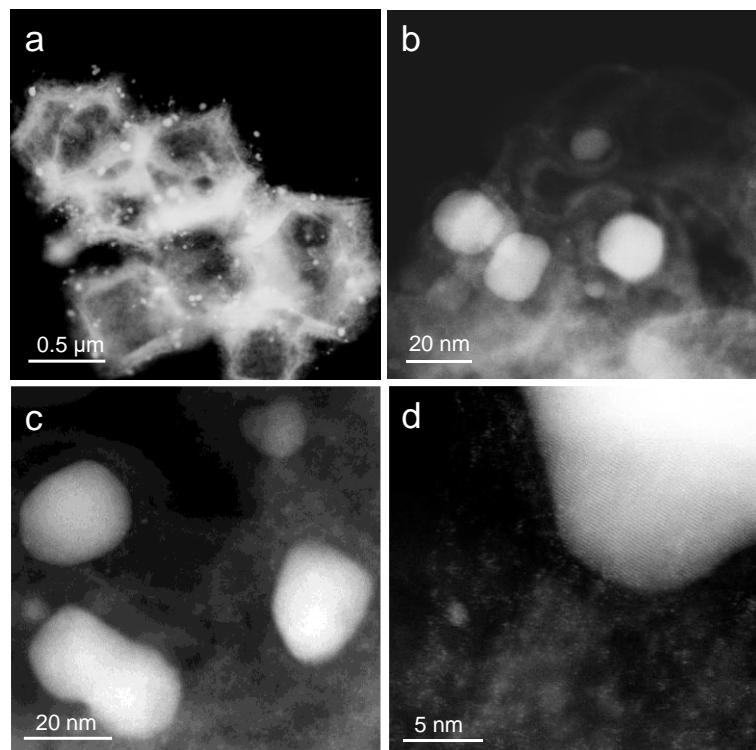


Fig. S37. HAADF-STEM images of $\text{Co}_n\text{-Pt}_1@\text{N}_{[5]/[6]} \text{C}$.

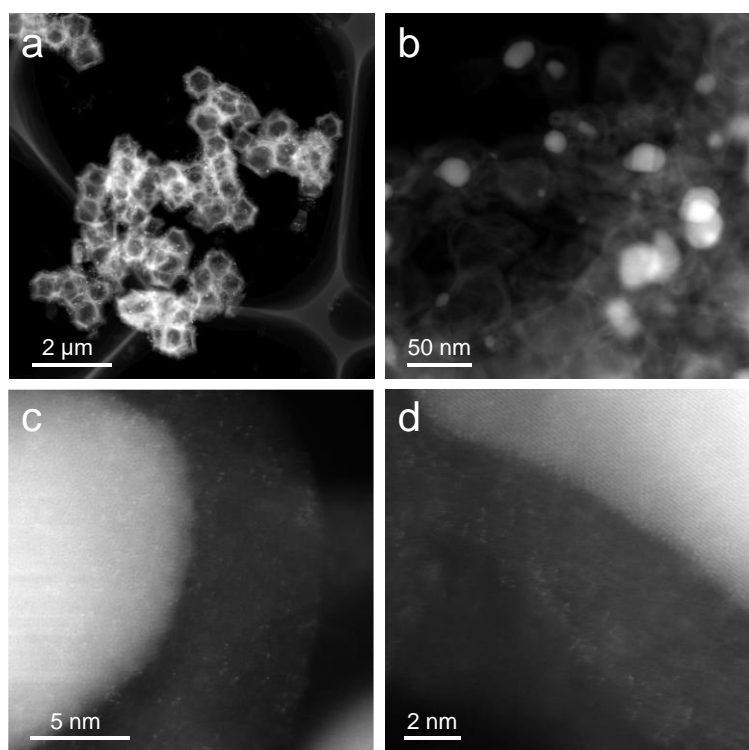


Fig. S38. HAADF-STEM images of $\text{Co}_n\text{-Pt}_1@\text{N}_{[5]/[6]} \text{C}$.

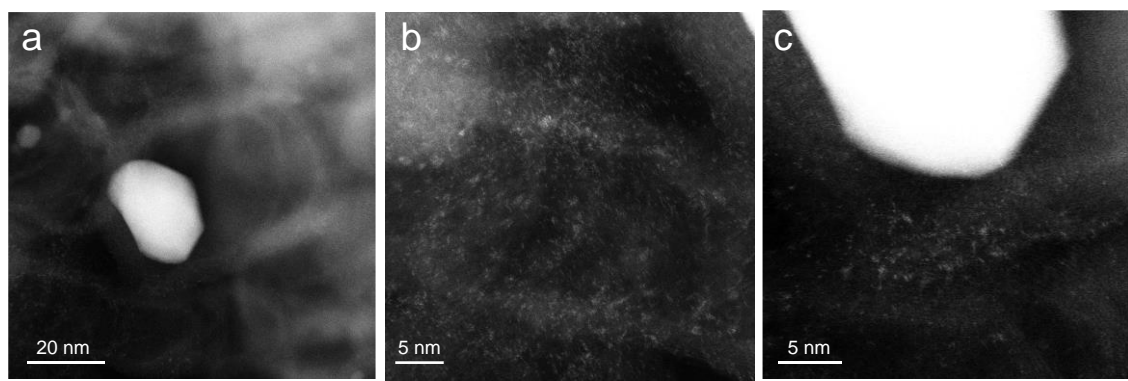


Fig. S39. HAADF-STEM images of $\text{Co}_n\text{-Pt}_1@\text{N}_{[5]/[6]} \text{C}$.

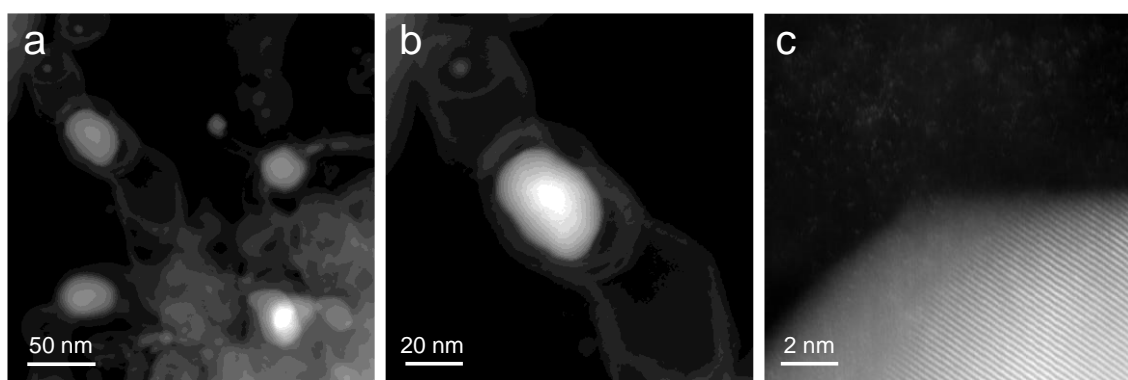


Fig. S40. HAADF-STEM images of $\text{Co}_n\text{-Pt}_1@\text{N}_{[5]/[6]} \text{C}$.

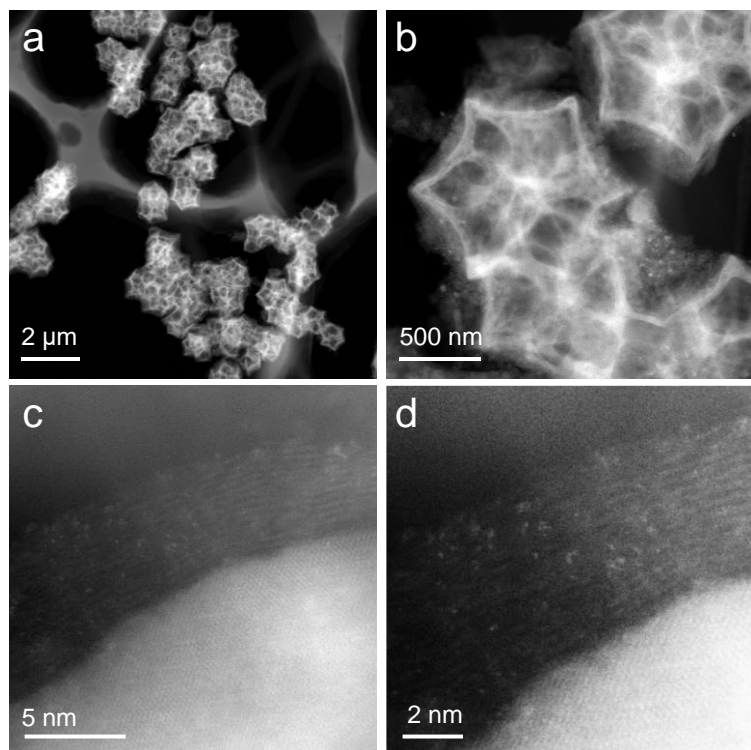


Fig. S41. HAADF-STEM images of $\text{Co}_n\text{-Pt}_1@\text{N}_{[6]}\text{C}$.

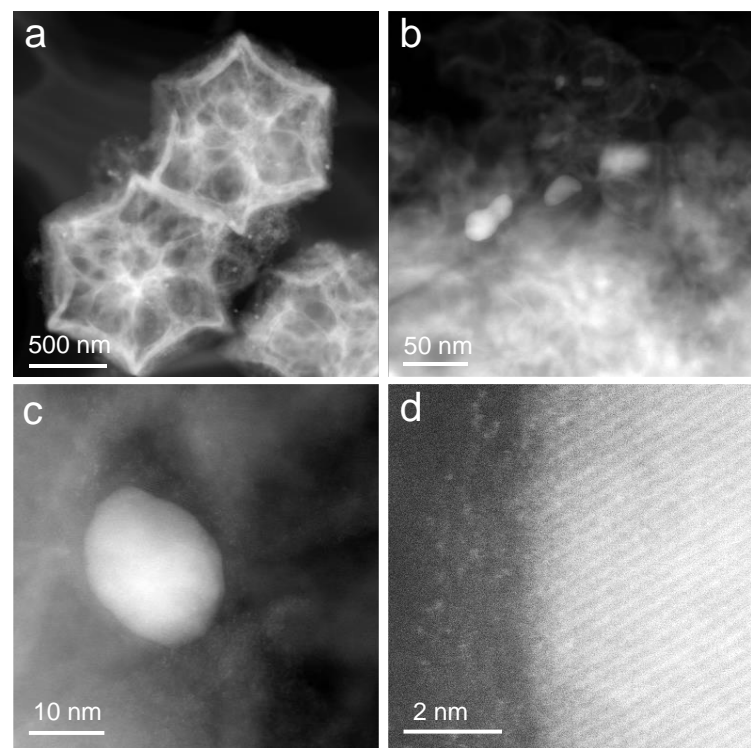


Fig. S42. HAADF-STEM images of $\text{Co}_n\text{-Pt}_1@\text{N}_{[6]}\text{C}$.

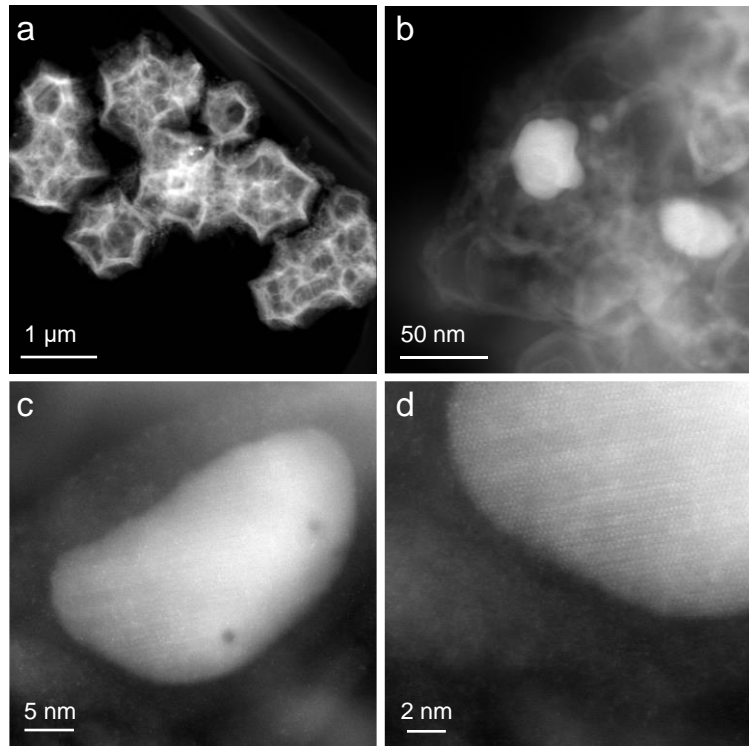


Fig. S43. HAADF-STEM images of $\text{Co}_n\text{-Pt}_1@\text{N}_{[6]}\text{C}$.

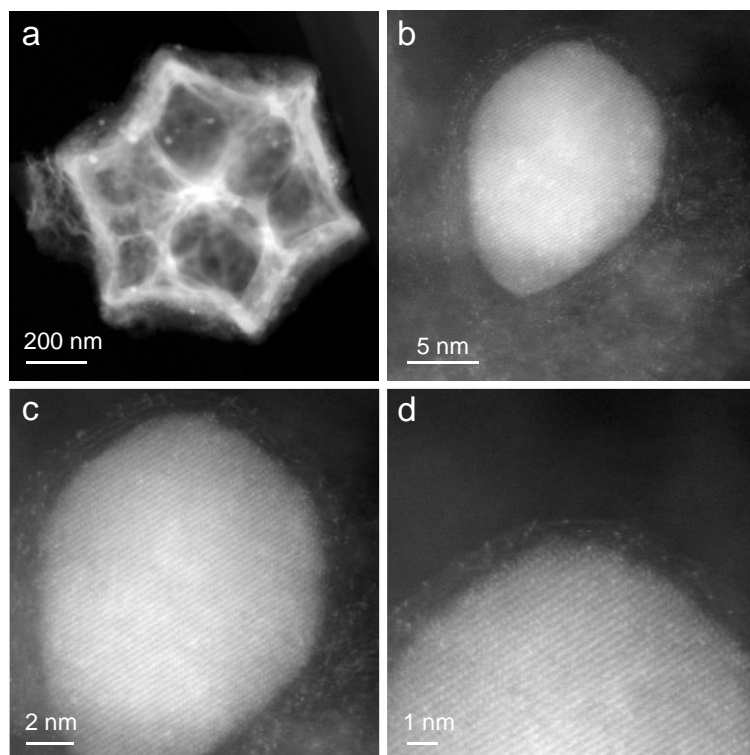


Fig. S44. HAADF-STEM images of $\text{Co}_n\text{-Pt}_1@\text{N}_{[6]}\text{C}$.

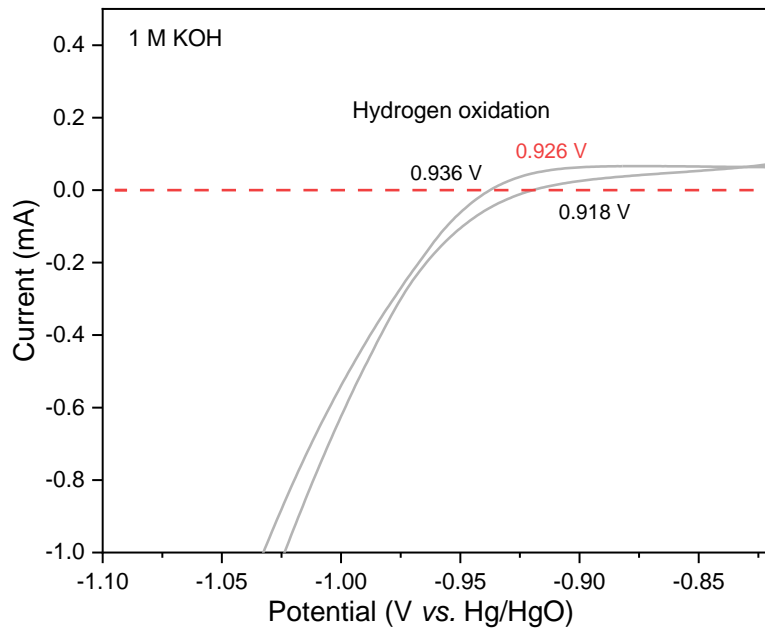


Fig. S45. Potential calibration of the reference electrode concerning reversible hydrogen electrode (RHE). It was performed in the high-purity hydrogen (99.99% H₂) saturated electrolyte with a Pt wire as the working electrode. In 1 M KOH, cycle voltammetry from -0.7 ~ -1.1 V was done with a scan rate of 2 mV s⁻¹, where the current crossed zero is taken to be the thermodynamic potential (vs. Hg/HgO) for the hydrogen evolution, E (vs. RHE) = E (vs. Hg/HgO) + 0.926 V.

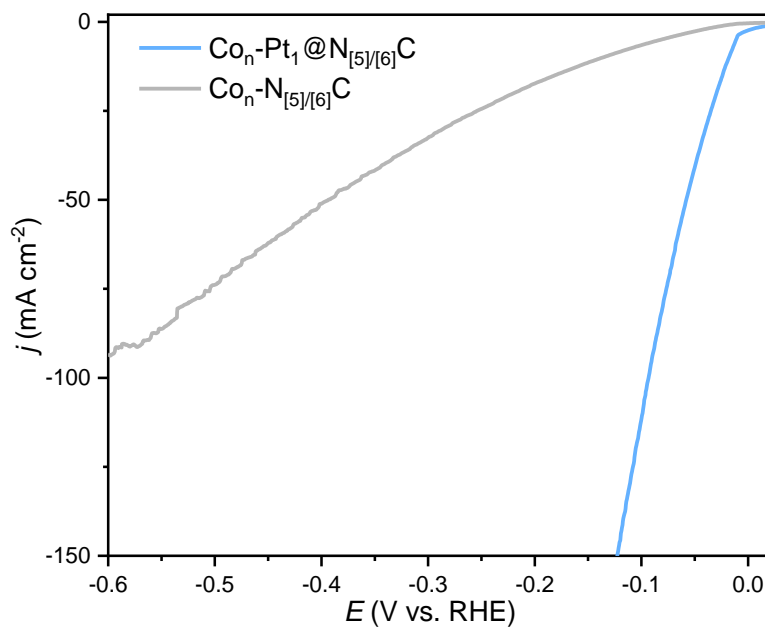


Fig. S46. HER polarization curves of Co_n-Pt₁@N_{[5]/[6]}C and Co_n-N_{[5]/[6]}C.

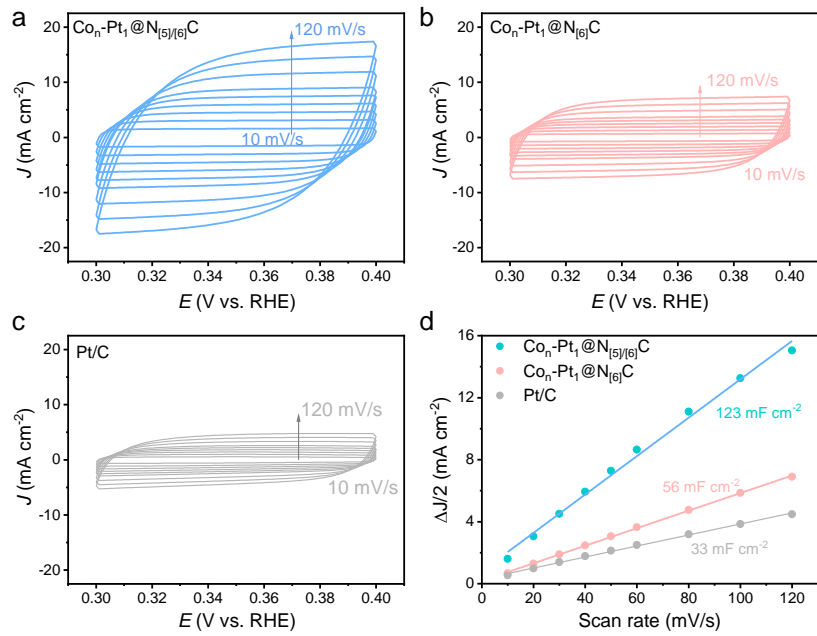


Fig. S47. CV curves of (a) $\text{Co}_n\text{-Pt}_1@\text{N}_{[5]/[6]} \text{C}$ (b) $\text{Co}_n\text{-Pt}_1@\text{N}_{[6]} \text{C}$, (c) 20% Pt/C at different scanning rates, (d) The calculated C_{dl} for three catalysts.

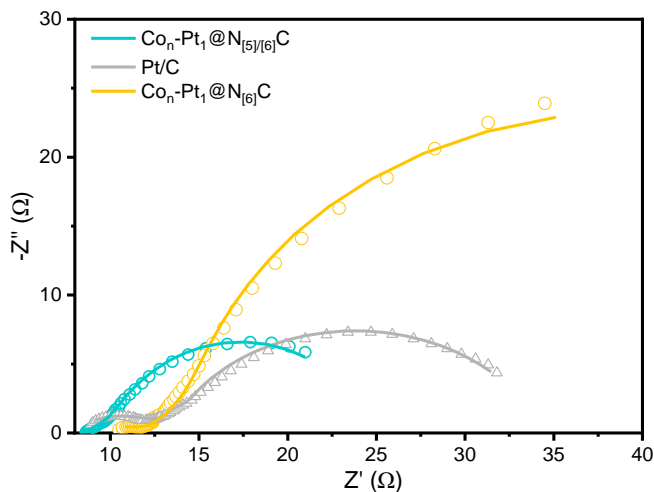


Fig. S48. Electrochemical impedance spectroscopy (EIS) curve of $\text{Co}_n\text{-Pt}_1@\text{N}_{[5]/[6]} \text{C}$, 20%Pt/C, and $\text{Co}_n\text{-Pt}_1@\text{N}_{[6]} \text{C}$.

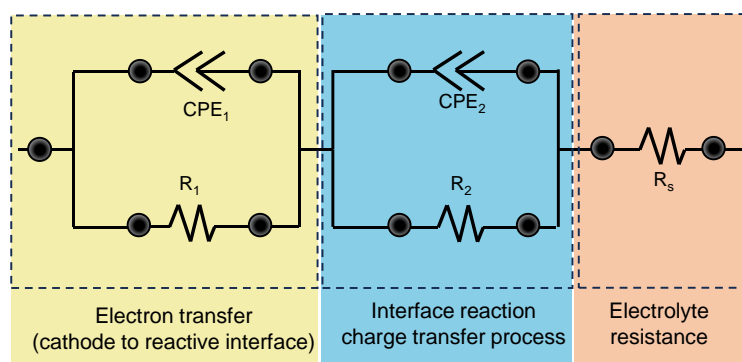


Fig. S49. The equivalent circuits for HER of $\text{Co}_n\text{-Pt}_1@\text{N}_{[5]/[6]} \text{C}$ in 1 M KOH (Tafel slope < 30).¹⁵

The parallel circuit includes one resistor (R_1) and one constant phase element (CPE_1), corresponding to the inner layer of catalysts, where R_1 is the charge transfer resistance and CPE_1 corresponds to the double-layer capacitance. The second section of a parallel circuit containing resistance (R_2) and constant phase element (CPE_2) corresponds to interface reaction charge transfer (the electrochemical desorption of H^*). R_s is electrolyte resistance.

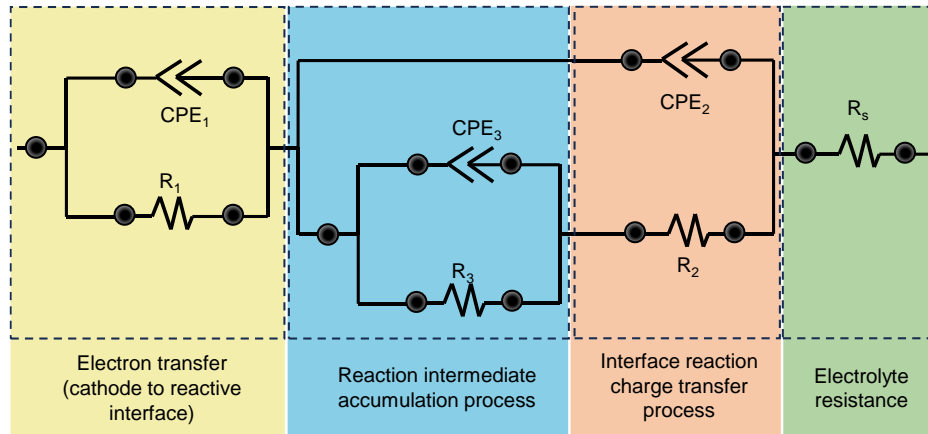


Fig. S50. The equivalent circuits for HER of catalysis in 1 M KOH (Tafel slope>30).

The parallel circuit includes one resistor (R_1) and one constant phase element (CPE_1), corresponding to the inner layer of catalysts, where R_1 is the charge transfer resistance and CPE_1 corresponds to the double-layer capacitance. The second section of a parallel circuit containing resistance (R_2) and constant phase element (CPE_2) corresponds to interface reaction charge transfer (the electrochemical desorption of H^*). The third parallel circuit simulates the electrolyte-catalyst interfacial charge transfer, which can reflect the hydrogen intermediate adsorption behavior on the catalytically active sites. R_3 is the ion transfer resistance and CPE_3 represents the hydrogen adsorption pseudo-capacitance. CPE_3 as a function of overpotential was integrated to calculate the hydrogen adsorption charge (Q_{H^*}). R_s is electrolyte resistance.

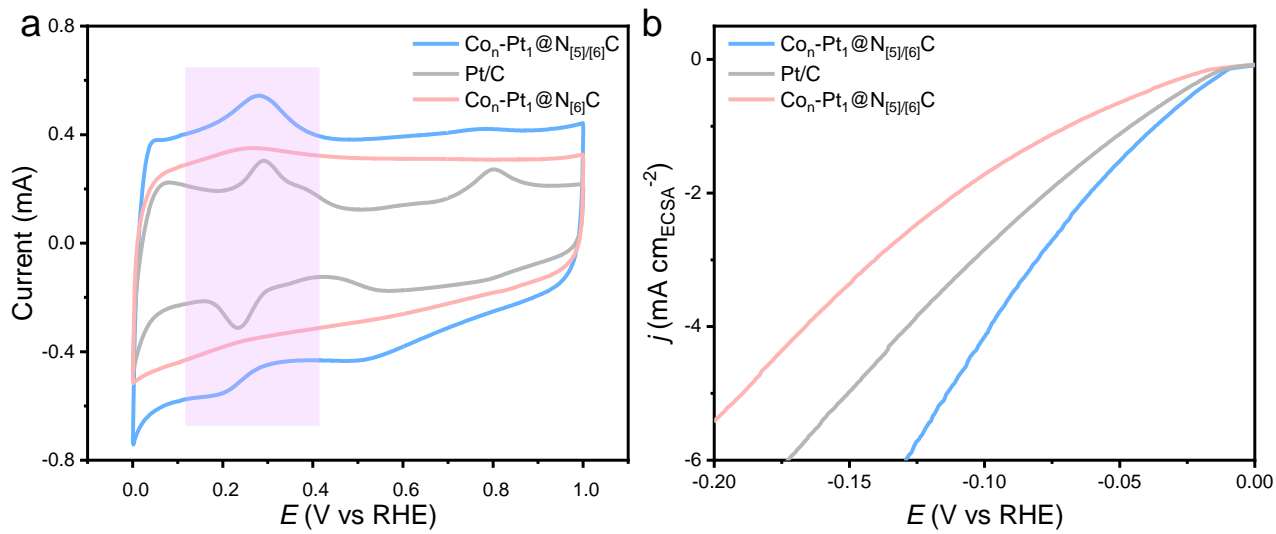


Fig. S51 (a) Cyclic voltammetry curves of $\text{Co}_n\text{-Pt}_1@\text{N}_{[5]/[6]}\text{C}$, $\text{Co}_n\text{-Pt}_1@\text{N}_{[6]}\text{C}$, and Pt/C in Ar-saturated 1 M KOH with a scan rate of 50 mV s⁻¹; (b) j_{ECSA} of various catalysts as a function of applied potential.

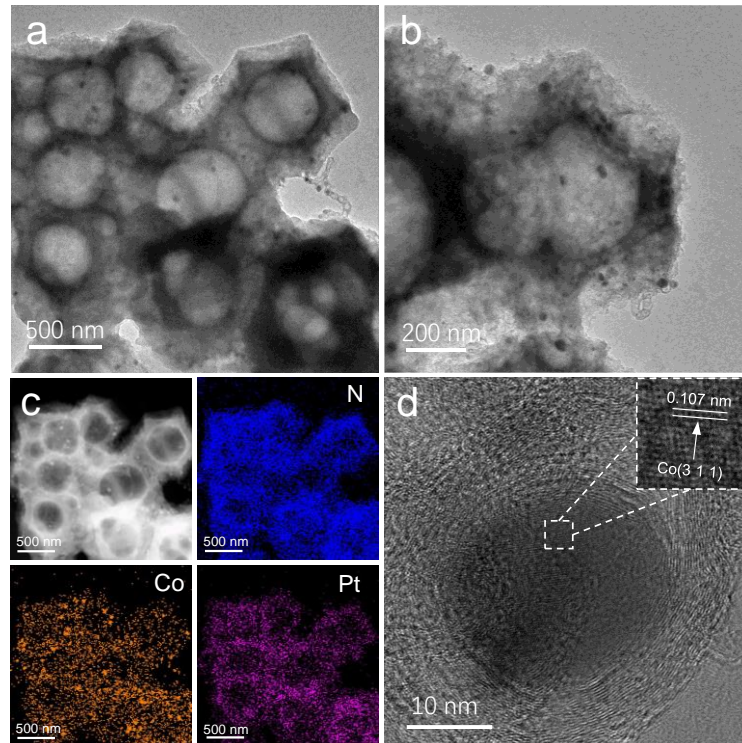


Fig. S52. TEM (a, b), EDS mapping (c), and (d) HRTEM images of $\text{Co}_n\text{-Pt}_1@\text{N}_{[5]/[6]}\text{C}$ after 100 h stability testing.

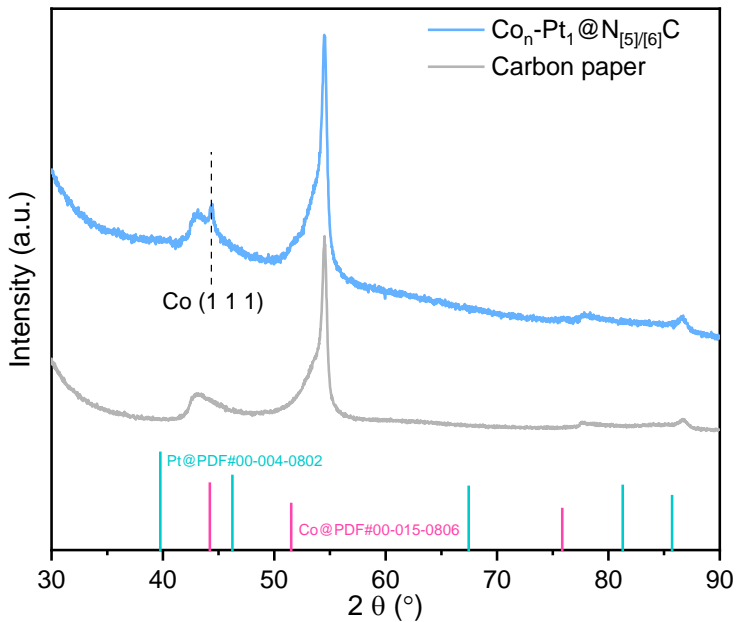


Fig. S53. XRD patterns of 100 h-stability-tested $\text{Co}_n\text{-Pt}_1\text{@N}_{[5]/[6]} \text{C}$ and pristine carbon paper.

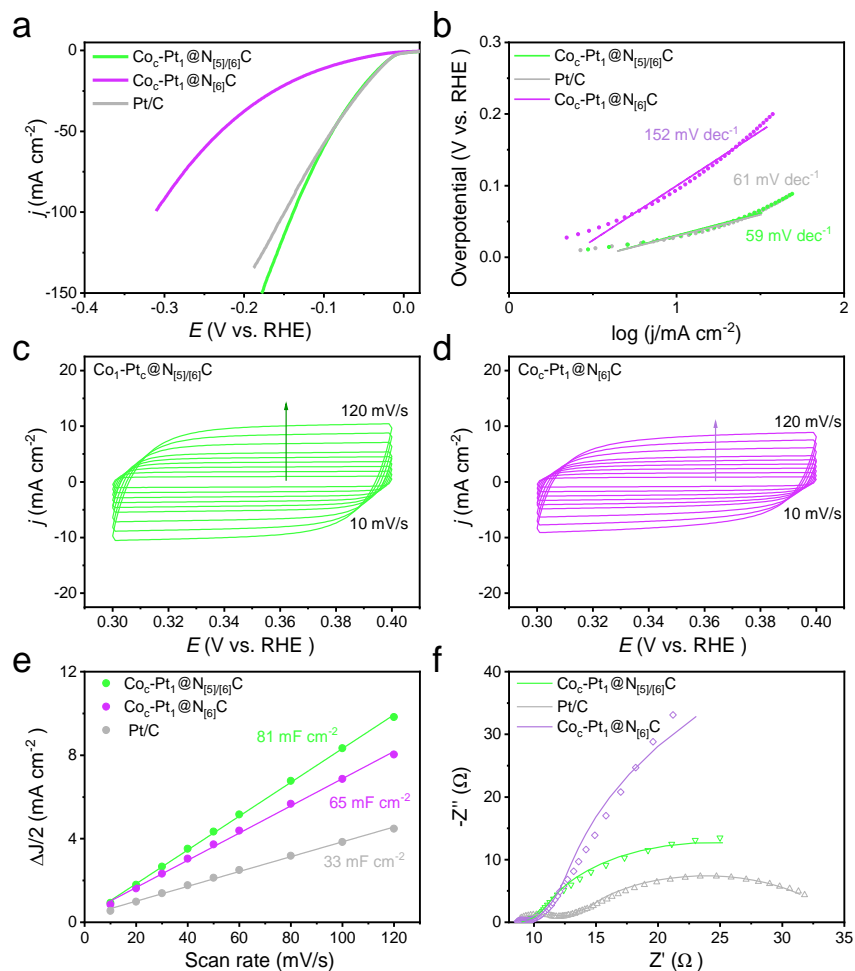


Fig. S54. HER performance of $\text{Co}_c\text{-Pt}_1\text{@N}_{[5]/[6]} \text{C}$, 20%Pt/C, and $\text{Co}_c\text{-Pt}_1\text{@N}_{[6]} \text{C}$ in alkaline. (a) HER polarization curves, (b) Tafel plots, (c) CV curves of $\text{Co}_c\text{-Pt}_1\text{@N}_{[5]/[6]} \text{C}$, (d) CV curves of $\text{Co}_c\text{-Pt}_1\text{@N}_{[6]} \text{C}$ at different scan rates, (e) Corresponding evaluation of C_{dl} values, (f) EIS curves.

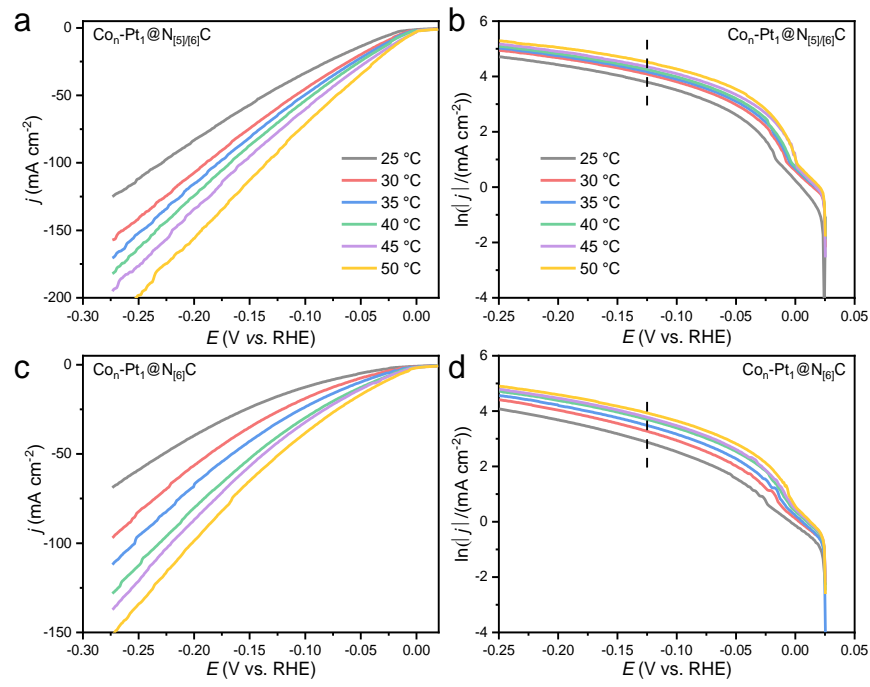


Fig. S55. Polarization curves (a, c) and Tafel plots (b, d) under a certain temperature range of 25-50 °C for $\text{Co}_n\text{-Pt}_1@\text{N}_{[5]/[6]} \text{C}$ and $\text{Co}_n\text{-Pt}_1@\text{N}_{[6]} \text{C}$, respectively.

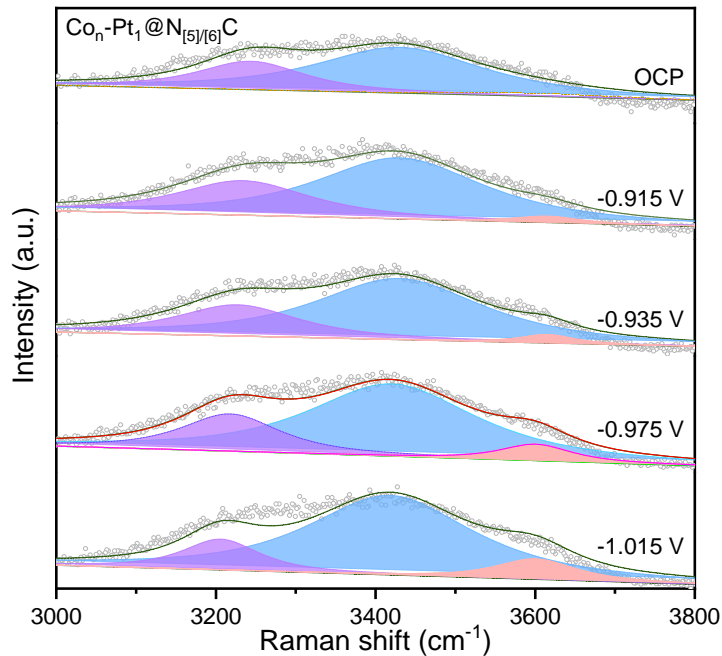


Fig. S56. *In-situ* electrochemical Raman spectra of interface adsorbed water at $\text{Co}_n\text{-Pt}_1@\text{N}_{[5]/[6]} \text{C}$ surface.

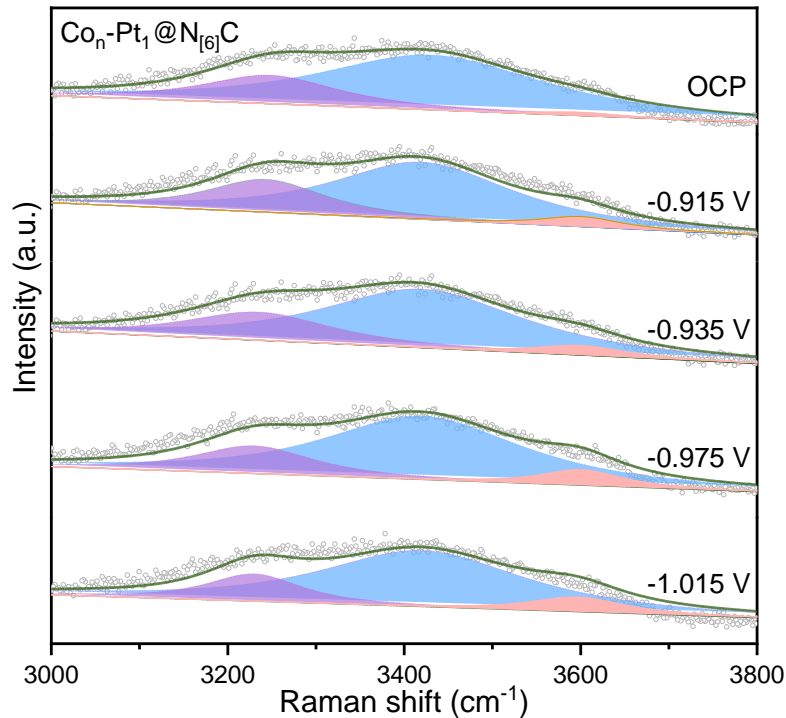


Fig. S57. *In-situ* Raman spectra electrochemical Raman spectra of interface adsorbed water at $\text{Co}_n\text{-Pt}_1\text{@N}_{[6]}\text{C}$ surface.

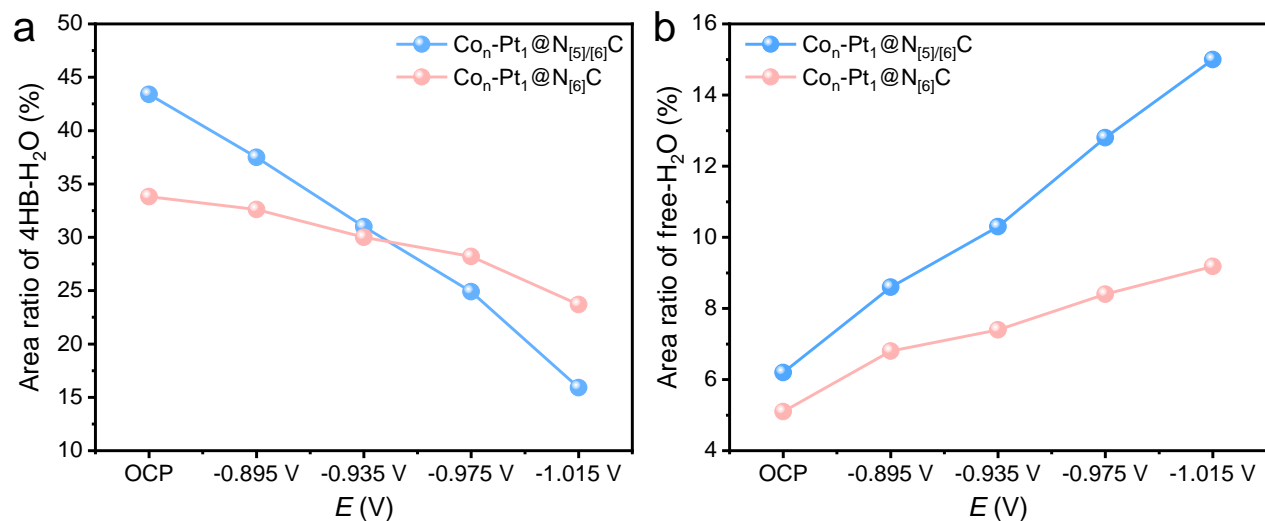


Fig. S58. Raman area ratios of the (a) 4HB- H_2O and (b) free- H_2O at $\text{Co}_n\text{-Pt}_1\text{@N}_{[5]/[6]}\text{C}$ and $\text{Co}_n\text{-Pt}_1\text{@N}_{[6]}\text{C}$ surface. Generally, the activation energy of water dissociation follows the sequence: free- H_2O <2-coordinated hydrogen-bonded water ($2\text{HB-}\text{H}_2\text{O}$)<4HB- H_2O , indicating that 4HB- H_2O can transform into 2HB- H_2O and free- H_2O with increasing potential.^{16,17} As the applied potential becomes more negative, the area ratio of the 4HB- H_2O exhibits a sharp decline, whereas the area ratio of free- H_2O experiences a rapid increase (**Fig. S58**).

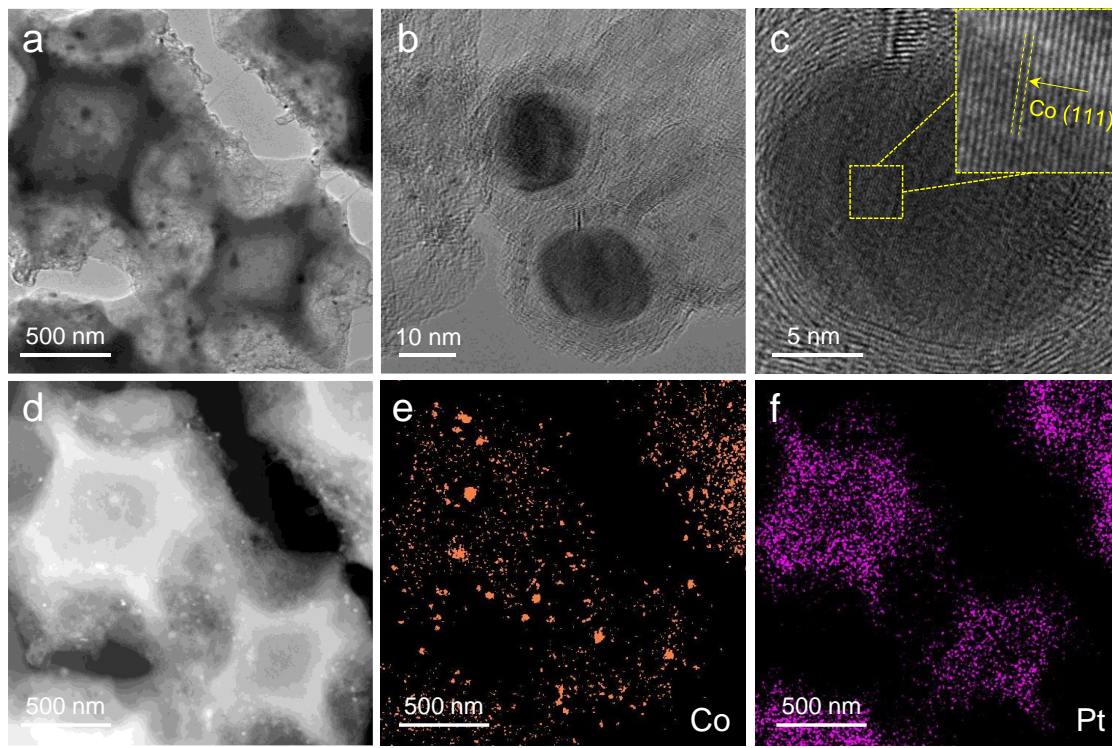


Fig. S59. TEM images (**a-c**) and EDS elemental mappings (**d-f**) of $\text{Co}_n\text{-Pt}_1\text{@N}_{[5]\text{/[6]}\text{C}$ after 400 h AEMWE stability testing.

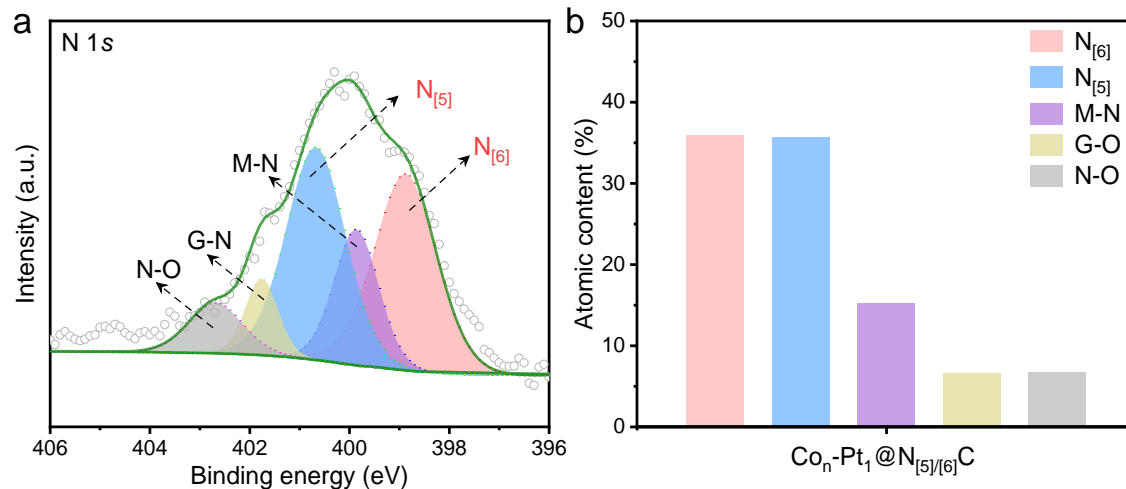


Fig. S60. **(a)** High-resolution XPS spectra of N 1s for $\text{Co}_n\text{-Pt}_1\text{@N}_{[5]\text{/[6]}\text{C}$ after 400 h AEMWE stability testing. **(b)** Corresponding contents of N_[6], N_[5], G-N, and O-N in $\text{Co}_n\text{-Pt}_1\text{@N}_{[5]\text{/[6]}\text{C}$.

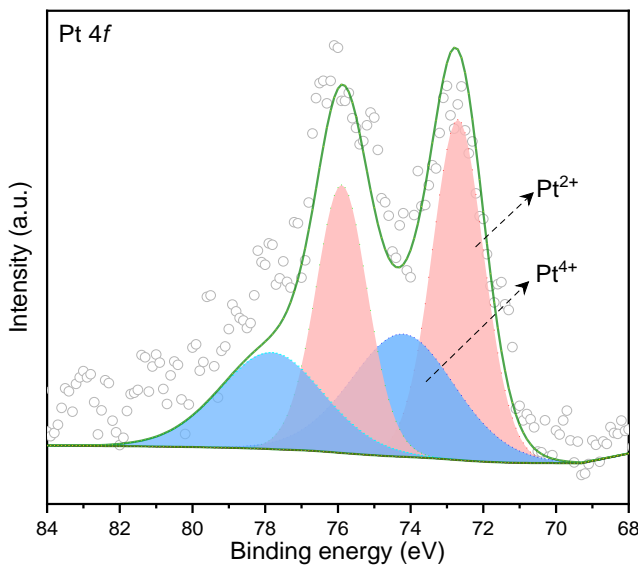


Fig. S61. High-resolution XPS spectra of Pt 4f for $\text{Co}_n\text{-Pt}_1@\text{N}_{[5]/[6]}\text{C}$ after 400 h AEMWE stability testing.

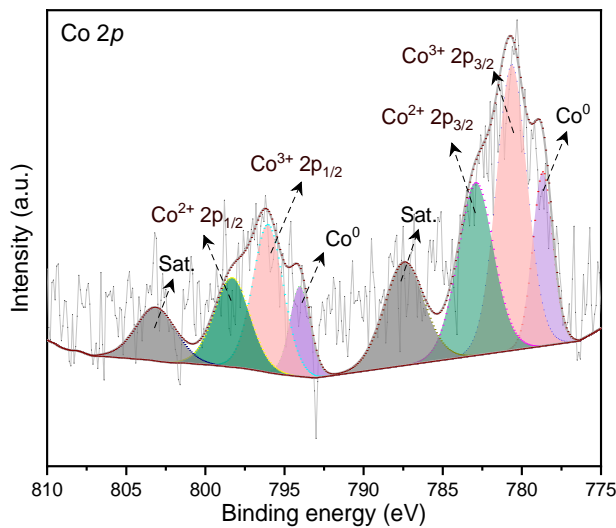


Fig. S62. High-resolution XPS spectra of Co 2p for $\text{Co}_n\text{-Pt}_1@\text{N}_{[5]/[6]}\text{C}$ after 400 h AEMWE stability testing.

Transmission electron microscopy (TEM) analysis (**Fig. S59a-d**) demonstrates the structural integrity and spatial retention of Co nanoparticles following prolonged AEMWE operation, with no observable morphological degradation or particle agglomeration. Elemental mapping analysis (**Fig. S59e-f**) confirms the homogeneous dispersion of Pt species at atomic scales. These findings were further corroborated by X-ray photoelectron spectroscopy (XPS), which reveal no significant shifts in Pt 4f binding energy signatures or alterations to the N-coordination environment ($\text{N}_{[5]}/\text{N}_{[6]}$ ratios), thereby confirming the electrochemical stability of both Pt single-atom active sites, Co nanoparticles and the nitrogen-doped carbon matrix under operational HER conditions. Collectively, these post-characterizations validate the robustness of the catalyst architecture and its resistance to reconstruction under reactive potentials (**Fig. S60-62**).

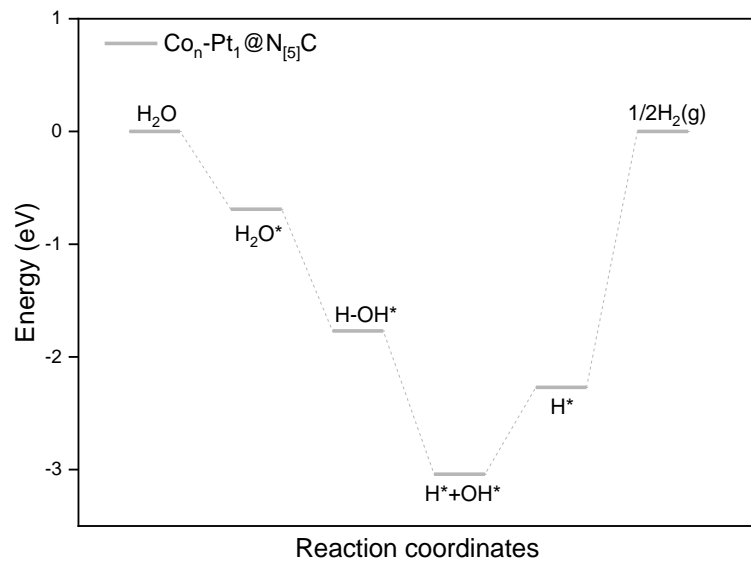


Fig. S63. Gibbs free energy diagram of the alkaline HER process on $\text{Co}_n\text{-Pt}_1@\text{N}_{[5]}\text{C}$.

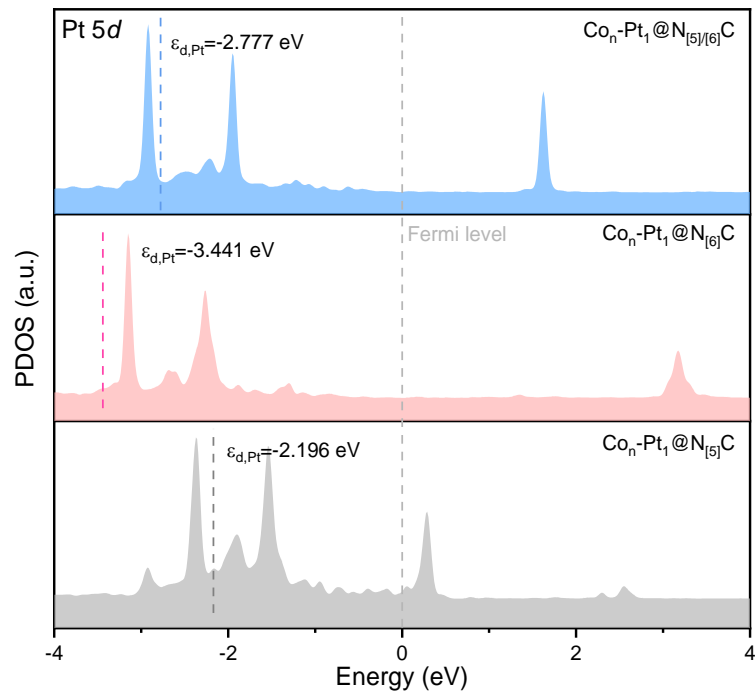


Fig. S64. Calculated PDOS of Pt 5d for $\text{Co}_n\text{-Pt}_1@\text{N}_{[5]/[6]}\text{C}$, $\text{Co}_n\text{-Pt}_1@\text{N}_{[6]}\text{C}$, and $\text{Co}_n\text{-Pt}_1@\text{N}_{[5]}\text{C}$. The d -band center of Pt in $\text{Co}_n\text{-Pt}_1@\text{N}_{[5]}\text{C}$ is significantly close to the Fermi level, indicating extremely strong H^* adsorption, which could impede the desorption of H^* .

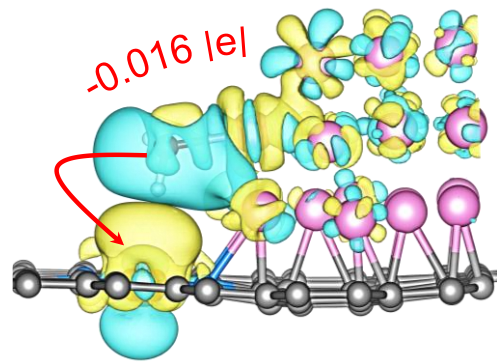


Fig. S65. Differential charge density image of water adsorption on $\text{Co}_n\text{-Pt}_1@\text{N}_{[5]}\text{C}$; the yellow and blue regions represent charge accumulation and decrease, respectively.

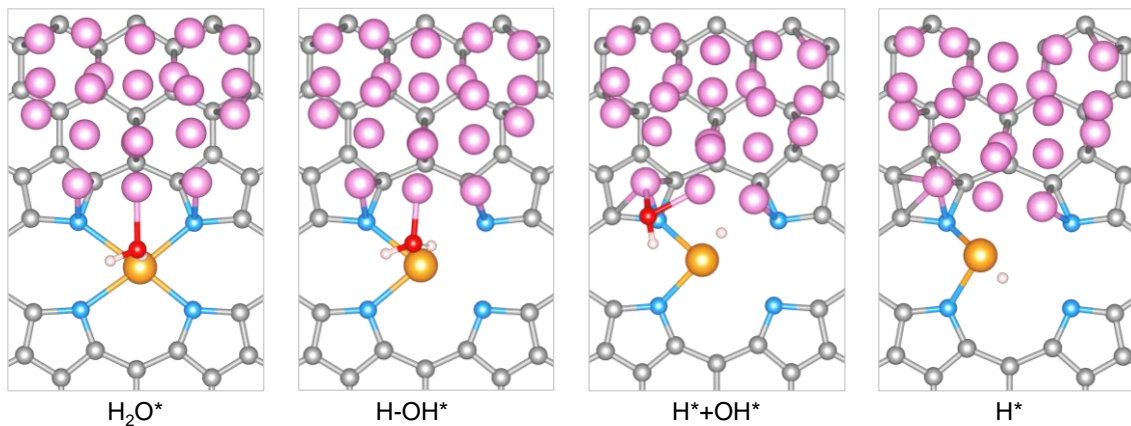


Fig. S66. Water splitting model for $\text{Co}_n\text{-Pt}_1@\text{N}_{[5]}\text{C}$. The white, gray, blue, red, purple, and orange spheres represent H, C, N, O, Co, and Pt atoms, respectively. Due to the instability of this structure, it underwent degradation during the water-splitting process.

Table S1. Recent advances in the regulation of types of N in single-atom catalysts.

Atoms	Type of N ^a	Adjustment ^b	Application ^c	Ref
Ni	Pyrrolic-N	Nitrogen source (C_3N_4)	CO ₂ RR	¹⁸
Fe	Pyrrolic-N	Nitrogen source (1, 10-phenanthroline)	Fenton-like reactions	¹⁹
Cu	Pyridine-N	Nitrogen source (PPy-PEI hydrogels)	NO ₃ RR	²⁰
Mo	Pyrrolic-N	Nitrogen source (PDA)	OER (Mo-pyrrolic-N)	²¹
	Pyridine-N		ORR (Mo-Pyridine-N)	
Pt	Pyrrolic-N	Nitrogen source (CNT)	HER	²²
Pt	Graphitic-N	Nitrogen source (glycine or ammonia)	ORR	²³
Co	Pyrrolic-N	Nitrogen source ($C_7H_{10}N$, $C_4H_6N_2$, and $C_2H_4N_4$)	ORR (2e ⁻)	²⁴
Zn	Edge-N	Pyrolysis atmosphere	Fenton-like reactions	²⁵
Fe	Pyridine-N	Pyrolysis atmosphere	ORR	²⁶
Mn	Pyrrolic-N	Pyrolysis atmosphere	ORR	²⁷

^a The table indicates that the reported literature primarily focuses on achieving high proportions of single N-type regulation.

^b PDA: Polydopamine; PPy-PEI: Poly-Polyetherimide; CNT: Carbon Nanotubes.

^c CO₂RR: CO₂ reduction reaction; OER: Oxygen Evolution Reaction; ORR: Oxygen Reduction Reaction; NO₃RR: NO₃ Reduction Reaction.

Table S2. Structural parameters of Pt foil and Co_n-Pt₁@NC extracted from the EXAFS fitting

Sample	Bond type	CN	R (Å)	σ^2 (10 ⁻³ Å ²)	R factor
Co _n -Pt ₁ @N _{[5]/[6]} C	Pt-N	3.9±0.1	2.26±0.01	1.9±1.2	0.015
Co _n -Pt ₁ @N _[6] C	Pt-N	3.8±0.2	2.25±0.02	1.5±0.8	0.011
Pt foil	Pt-Pt	12	2.76±0.01	4.5±0.2	0.003

Note: CN, coordination number; R, distance between the coordination atoms; σ^2 , Debye-Waller factors; R factor (%) indicates the goodness of the fit. S_0^2 was fixed to 0.85 as determined from Pt foil fitting.

Table S3. Specific surface area, pore volume, and pore diameter information of Co_n@N_{5/6}C, Co_n@N₆C, Co_n-Pt₁@N_{5/6}C, and Co_n-Pt₁@N₆C.

Materials	BET Surface	Langmuir Surface	Total pore	Micropore	Average pore
	Area (m ² /g)	Area (m ² /g)	volume (cm ³ /g)	volume (cm ³ /g)	diameter (nm)
Co _n @N _{[5]/[6]} C	600.72	980.46	0.484	0.225	7.91
Co _n @N _[6] C	144.36	410.05	0.331	0.040	15.80
Co _n -Pt ₁ @N _{[5]/[6]} C	515.97	859.91	0.417	0.193	7.59
Co _n -Pt ₁ @N _[6] C	134.31	401.86	0.283	0.037	14.95

Table S4. Optimum fit parameters for the impedance data during HER in 1 M KOH.

Materials	R_s/Ω	R_1/Ω	CPE_1/F	R_2/Ω	CPE_2/F	R_3/Ω	CPE_3/F
Co _n -Pt ₁ @N _{5/6} C	8.625	2.07	0.0099	14.82	0.00018	---	---
Co _n -Pt ₁ @N ₆ C	9.73	2.9	0.000028	73.5	0.0003	9.749	0.018
Pt/C	8.375	3.315	0.000009	21.94	0.0035	7.252	0.058
Co ₁ -Pt ₁ @N _{5/6} C	8.842	1.643	0.0015	29.39	0.0002	2.858	0.033
Co ₁ -Pt ₁ @N ₆ C	8.647	1.825	0.000004	90.25	0.004	31.33	0.05

Table S5. Comparison of the HER performance with other state-of-the-art noble-metal single-atom HER electrocatalysts in alkaline.

Samples*	Atom	Loading (wt%)	Electrolyte (KOH)	Tafel slope (mV dec ⁻¹)	Overpotential (mV at η10)	Journal	Ref.
Pt ₁ -NiCoP@MXene	Pt	1	1 M	38.6	26.5	<i>Angew. Chem. Int. Edit.</i> 2024	²⁸
2D-Pt ₁ /LDH	Pt	56	1 M	32.3	23	<i>Adv. Mater.</i> 2022	²⁹
Pt ₁ /Mn ₃ O ₄	Pt	5.0	1 M	54	24	<i>Energ. Environ. Sci.</i> 2022	³⁰
Pt-ACs/CoNC	Pt	0.52	1 M	-	50	<i>Nat. Commun.</i> 2022	³¹
Pt ₁ /NMHCS	Pt	1.59	1 M	56	41	<i>Adv. Mater.</i> 2021	³²
Pt ₁ /CoHPO	Pt	0.57	0.1 M	38.5	49	<i>Nat. Commun.</i> 2022	³³
Pt ₁ @Fe-N-C	Pt	2.1	0.1 M	60	105	<i>Adv. Energy Mater.</i> 2018	³⁴
CoPt-PtSA/NDPCF	Pt	0.281	1 M	31	31	<i>Adv. Funct. Mater.</i> 2022	³⁵
NGA-COF@P	Pt	2.66	1 M	24	19	<i>Nat. Commun.</i> 2024	³⁶
PtSA-Co(OH) ₂	Pt	2.8	1 M	35	29	<i>Energ. Environ. Sci.</i> 2020	³⁷
Pt@CoN ₄ -G	Pt	2.83	1 M	29	39	<i>Adv. Funct. Mater.</i> 2023	³⁸
Pt/MVF	Pt	1.79	1 M	28	24	<i>Nano Lett.</i> 2022	³⁹
Pt/C60	Pt	21	1 M	55	25	<i>Nat. Commun.</i> 2023	⁴⁰
Pt-Ru/RuO ₂	Pt	1.36	1 M	18.5	18	<i>Nat. Commun.</i> 2024	⁴¹
PtSA-NiO/Ni	Pt	1.14	1M	27	26	<i>Nat. Commun.</i> 2021	⁴²
Co _n -Pt ₁ @N _{[5][6]} C	Pt	8.38	1 M	28	17	This work	

Table S6. Quantitative ICP-OES analysis of Co loading in $\text{Co}_n @\text{NC}$ and $\text{Co}_n\text{-}\text{Pt}_1@\text{NC}$.

Materials	Co (wt.%) ^a
$\text{Co}_n@\text{N}_{[5]/[6]}\text{C}$	4.4
$\text{Co}_n@\text{N}_{[6]}\text{C}$	5.95
$\text{Co}_n\text{-}\text{Pt}_1@\text{N}_{[5]/[6]}\text{C}$	3.98
$\text{Co}_n\text{-}\text{Pt}_1@\text{N}_{[6]}\text{C}$	5.18

^a Due to the large specific surface area of $\text{Co}_n@\text{N}_{[5]/[6]}\text{C}$, during the pickling process, a relatively large number of Co particles were etched away because of their large contact area with the liquid.

Table S7. Comparison of AEMWE cell voltages using different cathodic catalysts.

Catalysts	Cell voltage (V @1A cm ⁻²)	Temperature (°C)	Journal	Reference
$\text{Co}_n\text{-}\text{Pt}_1@\text{N}_{[5]/[6]}\text{C}$	1.82	70	This work	
Ru ₁ -Mo ₂ C	1.83	65	<i>Energ. Environ. Sci.</i> , 2024	⁴³
Ru SAs/WC _x	1.79	80	<i>J. Am. Chem. Soc.</i> , 2024	⁴⁴
Pt-Ru/RuO ₂	1.90	60	<i>Nat. Commun.</i> , 2024	⁴¹
Pt-AC/Cr-N-C	1.90	80	<i>J. Am. Chem. Soc.</i> , 2023	⁴⁵
PtC ₆₀	2.01	60	<i>Nat. Commun.</i> , 2023	⁴⁶
UP-RuNi _{SAs} /C	1.95	70	<i>Nat. Commun.</i> , 2024	⁴⁷
Pt _{SAs} Ni	1.90	70	<i>J. Energy Chem.</i> , 2024	⁴⁸
Ru ₁ /PNC	1.94	60	<i>J. Am. Chem. Soc.</i> , 2025	⁴⁹
Pt-NiO _x -H ₂ /C	1.74	60	<i>Angew. Chem. Int. Ed.</i> 2025	⁵⁰
Cl-Pt/LDH	1.87	60	<i>Nat. Commun.</i> , 2022	⁵¹
Pt/NiCoP@MXene	1.78	60	<i>Angew. Chem. Int. Ed.</i> , 2024	⁵²
Pt-MoAl _{1-x} B	2.00	60	<i>Energy Environ. Sci.</i> , 2023	⁵³
Pt ₁ /CoHPO	1.80	80	<i>Nat. Commun.</i> , 2022	⁵⁴

Pt/C	2.04	60	<i>Int. J. Hydrog. Energy, 2022</i>	55
PtRu/C	1.63 @2 A cm ⁻²	60	<i>Nat. Energy, 2020</i>	56
PtSA-NiSe-V	2.05@500 mA cm ⁻²	25	<i>Angew. Chem.Int. Ed., 2023</i>	57

Reference

- 1 G. Kresse, J. Furthmüller, *Phys. Rev. B* 1996, **54**, 11169-11186.
- 2 G. Kresse, D. Joubert, *Phys. Rev. B* 1999, **59**, 1758-1775.
- 3 J.P. Perdew, K. Burke, M. Ernzerhof, *Phys. Rev. Lett.* 1996, **77**, 3865-3868.
- 4 S. Grimme, J. Antony, S. Ehrlich, H. Krieg, *The J. Chem. Phys.* 2010, **132**, 154104.
- 5 S. Grimme, S. Ehrlich, L. Goerigk, *J. Comput. Chem.* 2010, **32**, 1456-1465.
- 6 M. Yu, D.R. Trinkle, *J. Comput. Chem.* 2011, **134**, 064111.
- 7 A. Hjorth Larsen, J. Jørgen Mortensen, J. Blomqvist, I.E. Castelli, R. Christensen, M. Dułak, J. Friis, M.N. Groves, B. Hammer, C. Hargus, E.D. Hermes, P.C. Jennings, P. Bjerre Jensen, J. Kermode, J.R. Kitchin, E. Leonhard Kolsbjer, J. Kubal, K. Kaasbjerg, S. Lysgaard, J. Bergmann Maronsson, T. Maxson, T. Olsen, L. Pastewka, A. Peterson, C. Rostgaard, J. Schiøtz, O. Schütt, M. Strange, K.S. Thygesen, T. Vegge, L. Vilhelmsen, M. Walter, Z. Zeng, K.W. Jacobsen, *J. Phys. Condens. Mat.* 2017, **29**, 273002.
- 8 G. Henkelman, B.P. Uberuaga, H. Jónsson, *The J. Chem. Phys.* 2000, **113**, 9901-9904.
- 9 J.D. Kovac, *J. Chem. Educ.* 1998, **75**, 545.
- 10 V. Wang, N. Xu, J.-C. Liu, G. Tang, W.-T. Geng, *Comput. Phys. Commun.* 2021, **267**, 108033.
- 11 Y. Zheng, Y. Jiao, Y. Zhu, L.H. Li, Y. Han, Y. Chen, M. Jaroniec, S.-Z. Qiao, *J. Am. Chem. Soc.* 2016, **138**, 16174-16181.
- 12 J.K. Nørskov, T. Bligaard, A. Logadottir, J.R. Kitchin, J.G. Chen, S. Pandelov, U. Stimming, *J. Chem. Educ.* 2005, **152**, J23.
- 13 B.Y. Xia, Y. Yan, N. Li, H.B. Wu, X.W. Lou, X. Wang, *Nat. Energy* 2016, **1**, 15006.
- 14 Y. Pan, K. Sun, S. Liu, X. Cao, K. Wu, W.-C. Cheong, Z. Chen, Y. Wang, Y. Li, Y. Liu, D. Wang, Q. Peng, C. Chen, Y. Li, *J. Am. Chem. Soc.* 2018, **140**, 2610-2618.
- 15 W. Chen, B. Wu, Y. Wang, W. Zhou, Y. Li, T. Liu, C. Xie, L. Xu, S. Du, M. Song, D. Wang, Y. liu, Y. Li, J. Liu, Y. Zou, R. Chen, C. Chen, J. Zheng, Y. Li, J. Chen, S. Wang, *Energy Environ. Sci.* 2021, **14**, 6428-6440.
- 16 L.-f. Shen, B.-a. Lu, Y.-y. Li, J. Liu, Z.-c. Huang-fu, H. Peng, J.-y. Ye, X.-m. Qu, J.-m. Zhang, G. Li, W.-b. Cai, Y.-x. Jiang, S.-g. Sun, *Angew. Chem. Int. Edit.* 2020, **59**, 22397-22402.
- 17 W. Xia, M. Ma, Z. Li, L. Qiao, K. Chi, X. Guo, T. Liu, D. Wu, D. Cao, D. Cheng, *Appl. Catal. B: Environ. Energy* 2024, **354**, 124074.
- 18 R. Boppella, M. Austeria P, Y. Kim, E. Kim, I. Song, Y. Eom, D.P. Kumar, M. Balamurugan, E. Sim, D.H. Kim, T.K. Kim, *Adv. Funct. Mater.* 2022, **32**, 2202351.

- 19 Y. Xiong, H. Li, C. Liu, L. Zheng, C. Liu, J.-O. Wang, S. Liu, Y. Han, L. Gu, J. Qian, D. Wang, *Adv. Mater.* 2022, **34**, 2110653.
- 20 Y. Liu, W. Qiu, P. Wang, R. Li, K. Liu, K.M. Omer, Z. Jin, P. Li, *Appl. Catal. B: Environ.* 2024, **340**, 123228.
- 21 J. Balamurugan, P.M. Austeria, J.B. Kim, E.S. Jeong, H.H. Huang, D.H. Kim, N. Koratkar, S.O. Kim, *Adv. Mater.* 2024, **35**, 2302625.
- 22 L. Zhang, Q. Wang, R. Si, Z. Song, X. Lin, M.N. Banis, K. Adair, J. Li, K. Doyle-Davis, R. Li, L.-M. Liu, M. Gu, X. Sun, *Small* 2024, **17**, 2004453.
- 23 B. Ni, P. Shen, G. Zhang, J. Zhao, H. Ding, Y. Ye, Z. Yue, H. Yang, H. Wei, K. Jiang, *J. Am. Chem. Soc.* 2024, **146**, 11181-11192.
- 24 S. Chen, T. Luo, X. Li, K. Chen, J. Fu, K. Liu, C. Cai, Q. Wang, H. Li, Y. Chen, C. Ma, L. Zhu, Y.-R. Lu, T.-S. Chan, M. Zhu, E. Cortés, M. Liu, *J. Am. Chem. Soc.* 2022, **144**, 14505-14516.
- 25 X. Yu, H. Liu, Y. Huang, C. Li, L. Kuang, J. Zhong, S. Zhu, Y. Gou, Y. Wang, Y. Zhang, G. Shan, Z. Lv, S. Zhang, L. Zhu, *P. Natl. A. Sci.* 2023, **120**, e2221228120.
- 26 Y. Zeng, C. Li, B. Li, J. Liang, M.J. Zachman, D.A. Cullen, R.P. Hermann, E.E. Alp, B. Lavina, S. Karakalos, M. Lucero, B. Zhang, M. Wang, Z. Feng, G. Wang, J. Xie, D.J. Myers, J.-P. Dodelet, G. Wu, *Nat. Catal.* 2023, **6**, 1215-1227.
- 27 K. Kim, G. Kim, T. Jeong, W. Lee, Y. Yang, B.-H. Kim, B. Kim, B. Lee, J. Kang, M. Kim, *J. Am. Chem. Soc.* 2024, **146**, 34033-34042.
- 28 H.-J. Niu, C. Huang, T. Sun, Z. Fang, X. Ke, R. Zhang, N. Ran, J. Wu, J. Liu, W. Zhou, *Angew. Chem. Int. Edit.* 2024, **63**, e202401819.
- 29 T. Ma, H. Cao, S. Li, S. Cao, Z. Zhao, Z. Wu, R. Yan, C. Yang, Y. Wang, P.A. van Aken, L. Qiu, Y.-G. Wang, C. Cheng, *Adv. Mater.* 2022, **34**, 2206368.
- 30 J. Wei, K. Xiao, Y. Chen, X.-P. Guo, B. Huang, Z.-Q. Liu, *Energy Environ. Sci.* 2022, **15**, 4592-4600.
- 31 J. Zhang, M. Wang, Z. Gao, X. Qin, Y. Xu, Z. Wang, W. Zhou, D. Ma, *J. Am. Chem. Soc.* 2022, **144**, 5108-5115.
- 32 P. Kuang, Y. Wang, B. Zhu, F. Xia, C.-W. Tung, J. Wu, H.M. Chen, J. Yu, *Adv. Mater.* 2021, **33**, 2008599.
- 33 L. Zeng, Z. Zhao, F. Lv, Z. Xia, S.-Y. Lu, J. Li, K. Sun, K. Wang, Y. Sun, Q. Huang, Y. Chen, Q. Zhang, L. Gu, G. Lu, S. Guo, *Nat. Commun.* 2022, **13**, 3822.
- 34 X. Zeng, J. Shui, X. Liu, Q. Liu, Y. Li, J. Shang, L. Zheng, R. Yu, *Adv. Energy Mater.* 2018, **8**, 1701345.
- 35 W. Yang, P. Cheng, Z. Li, Y. Lin, M. Li, J. Zi, H. Shi, G. Li, Z. Lian, H. Li, *Adv. Funct. Mater.* 2022, **32**, 2205920.
- 36 Z. Zhang, Z. Zhang, C. Chen, R. Wang, M. Xie, S. Wan, R. Zhang, L. Cong, H. Lu, Y. Han, W. Xing, Z. Shi, S.

- Feng, *Nat. Commun.* 2024, **15**, 2556.
- 37 K.L. Zhou, C. Wang, Z. Wang, C.B. Han, Q. Zhang, X. Ke, J. Liu, H. Wang, *Energy Environ. Sci.* 2020, **13**, 3082-3092.
- 38 M. Zhang, H. Li, J. Chen, F.-X. Ma, L. Zhen, Z. Wen, C.-Y. Xu, *Adv. Funct. Mater.* 2023, **33**, 2303189.
- 39 Q. Liang, W. Li, L. Xie, Y. He, B. Qiu, H. Zeng, S. Zhou, J. Zeng, T. Liu, M. Yan, K. Liang, O. Terasaki, L. Jiang, B. Kong, *Nano Lett.* 2022, **22**, 2889-2897.
- 40 R. Zhang, Y. Li, X. Zhou, A. Yu, Q. Huang, T. Xu, L. Zhu, P. Peng, S. Song, L. Echegoyen, F.-F. Li, *Nat. Commun.* 2023, **14**, 2460.
- 41 Y. Zhu, M. Klingenhof, C. Gao, T. Koketsu, G. Weiser, Y. Pi, S. Liu, L. Sui, J. Hou, J. Li, H. Jiang, L. Xu, W.-H. Huang, C.-W. Pao, M. Yang, Z. Hu, P. Strasser, J. Ma, *Nat. Commun.* 2024, **15**, 1447.
- 42 K.L. Zhou, Z. Wang, C.B. Han, X. Ke, C. Wang, Y. Jin, Q. Zhang, J. Liu, H. Wang, H. Yan, *Nat. Commun.* 2021, **12**, 3783.
- 43 T. Chao, W. Xie, Y. Hu, G. Yu, T. Zhao, C. Chen, Z. Zhang, X. Hong, H. Jin, D. Wang, W. Chen, X. Li, P. Hu, Y. Li, *Energy Environ. Sci.* 2024, **17**, 1397-1406.
- 44 X. Lin, W. Hu, J. Xu, X. Liu, W. Jiang, X. Ma, D. He, Z. Wang, W. Li, L.-M. Yang, H. Zhou, Y. Wu, *J. Am. Chem. Soc.* 2024, **146**, 4883-4891.
- 45 L. Zeng, Z. Zhao, Q. Huang, C. Zhou, W. Chen, K. Wang, M. Li, F. Lin, H. Luo, Y. Gu, L. Li, S. Zhang, F. Lv, G. Lu, M. Luo, S. Guo, *J. Am. Chem. Soc.* 2023, **145**, 21432-21441.
- 46 J. Chen, M. Aliasgar, F.B. Zamudio, T. Zhang, Y. Zhao, X. Lian, L. Wen, H. Yang, W. Sun, S.M. Kozlov, W. Chen, L. Wang, *Nat. Commun.* 2023, **14**, 1711.
- 47 R. Yao, K. Sun, K. Zhang, Y. Wu, Y. Du, Q. Zhao, G. Liu, C. Chen, Y. Sun, J. Li, *Nat. Commun.* 2024, **15**, 2218.
- 48 R. Yao, Y. Wu, K. Zhang, S. Fan, Q. Zhao, J. Li, G. Liu, *J. Energy Chem.* 2024, **98**, 503-511.
- 49 H. Jin, X. Chen, Y. Da, L. Fan, R. Jiang, Y. Xiao, B. Yao, Q. He, Y. Yu, W. Chen, *J. Am. Chem. Soc.* 2025, **147**, 3874-3884.
- 50 X. Zheng, X. Zheng, M. Gao, Y. Liu, H. Pan, W. Sun, *Angew. Chem. Int. Edit.* 2025, **64**, e202422062.
- 51 T. Zhang, J. Jin, J. Chen, Y. Fang, X. Han, J. Chen, Y. Li, Y. Wang, J. Liu, L. Wang, *Nat. Commun.* 2022, **13**, 6875.
- 52 H.-J. Niu, C. Huang, T. Sun, Z. Fang, X. Ke, R. Zhang, N. Ran, J. Wu, J. Liu, W. Zhou, *Angew. Chem. Int. Edit.* 2024, **63**, e202401819.
- 53 S. J. Park, T. H. Nguyen, D. T. Tran, V. A. Dinh, J. H. Lee, N. H. Kim, *Energy Environ. Sci.* 2023, **16**, 4093-

4104.

- 54 L. Zeng, Z. Zhao, F. Lv, Z. Xia, S.-Y. Lu, J. Li, K. Sun, K. Wang, Y. Sun, Q. Huang, Y. Chen, Q. Zhang, L. Gu, G. Lu, S. Guo, *Nat. Commun.* 2022, **13**, 3822.
- 55 S. Y. Kang, J. E. Park, G. Y. Jang, O.-H. Kim, O. J. Kwon, Y.-H. Cho, Y.-E. Sung, *Int. J. Hydrot. Energy*, 2022 **47**, 9115-9126.
- 56 D. Li, E. J. Park, W. Zhu, Q. Shi, Y. Zhou, H. Tian, Y. Lin, A. Serov, B. Zulevi, E. D. Baca, C. Fujimoto, H. T. Chung, Y. S. Kim, *Nat. Energy* 2020, **5**, 378-385.
- 57 Z. Chen, X. Li, J. Zhao, S. Zhang, J. Wang, H. Zhang, J. Zhang, Q. Dong, W. Zhang, W. Hu, X. Han, *Angew. Chem. Int. Edit.* 2023, **62**, e202308686.